Mon. Not. R. Astron. Soc. **395,** 855–876 (2009) doi:10.1111/j.1365-2966.2009.14554.x

Properties of the ionized gas in HH 202 – II. Results from echelle spectrophotometry with Ultraviolet Visual Echelle Spectrograph⋆

A. Mesa-Delgado,[1]† C. Esteban,[1] J. García-Rojas,[2] V. Luridiana,[3] M. Bautista,[4] M. Rodríguez,[5] L. López-Martín[1] and M. Peimbert[2]

[1]*Instituto de Astrofísica de Canarias, E-38200 La Laguna, Tenerife, Spain*
[2]*Instituto de Astronomía, UNAM, Apdo. Postal 70-264, 04510 México D.F., Mexico*
[3]*Instituto de Astrofísica de Andalucía (CSIC), Apdo. Correos 3004, E-18080 Granada, Spain*
[4]*Deparment of Physics, Virginia Polytechnic and State University, Blacksburg, VA 24061, USA*
[5]*Instituto Nacional de Astrofísica, Óptica y Electrónica INAOE, Apdo. Postal 51 y 216, 7200 Puebla, Pue., Mexico*

Accepted 2009 January 23. Received 2008 December 23; in original form 2008 October 24

ABSTRACT

We present results of deep echelle spectrophotometry of the brightest knot of the Herbig–Haro object HH 202 in the Orion Nebula – HH 202-S – using the Ultraviolet Visual Echelle Spectrograph in the spectral range from 3100 to 10 400 Å. The high spectral resolution of the observations has permitted to separate the component associated with the ambient gas from that associated with the gas flow. We derive electron densities and temperatures from different diagnostics for both components, as well as the chemical abundances of several ions and elements from collisionally excited lines, including the first determinations of Ca^+ and Cr^+ abundances in the Orion Nebula. We also calculate the He^+, C^{2+}, O^+ and O^{2+} abundances from recombination lines. The difference between the O^{2+} abundances determined from collisionally excited and recombination lines – the so-called abundance discrepancy factor – is 0.35 and 0.11 dex for the shock and nebular components, respectively. Assuming that the abundance discrepancy is produced by spatial variations in the electron temperature, we derive values of the temperature fluctuation parameter, t^2, of 0.050 and 0.016 for the shock and nebular components, respectively. Interestingly, we obtain almost coincident t^2 values for both components from the analysis of the intensity ratios of He I lines. We find significant departures from case B predictions in the Balmer and Paschen flux ratios of lines of high principal quantum number n. We analyse the ionization structure of HH 202-S, finding enough evidence to conclude that the flow of HH 202-S has compressed the ambient gas inside the nebula trapping the ionization front. We measure a strong increase of the total abundances of nickel and iron in the shock component, the abundance pattern and the results of photoionization models for both components are consistent with the partial destruction of dust after the passage of the shock wave in HH 202-S.

Key words: ISM: abundances – dust, extinction – ISM: Herbig–Haro objects – ISM: individual: Orion Nebula – ISM: individual: HH 202.

1 INTRODUCTION

HH 202 is one of the brightest and most conspicuous Herbig–Haro (HH) objects of the Orion Nebula. It was discovered by Cantó et al. (1980). The origin of this outflow is not clear, though the radial velocity and proper motion studies suggest that this object forms a great complex together with HH 203, 204, 269, 529, 528 and 625, with a common origin in one or more sources embedded within the Orion Molecular Cloud 1 South (OMC 1S; see Rosado et al. 2002; O'Dell & Doi 2003; O'Dell & Henney 2008). Recently, Henney et al. (2007) have summarized the main characteristics of these outflows, and an extensive study of their kinematics can be found in García-Díaz et al. (2008). HH 202 shows a wide parabolic form with several bright knots of which HH 202-S is the brightest one (see Fig. 1).

The kinematic properties of HH 202-S have been studied by means of high spectral resolution spectroscopy by several authors.

⋆Based on observations collected at the European Southern Observatory, Chile, proposal number ESO 70.C-0008(A).

†E-mail: amd@iac.es

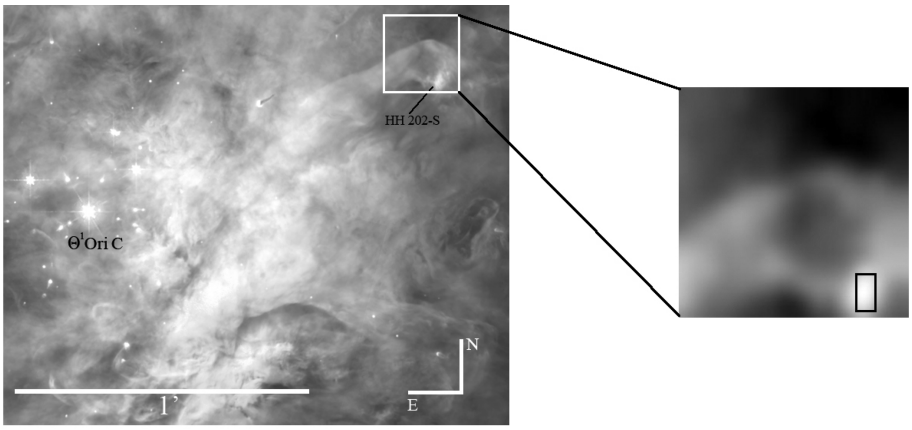

Figure 1. *HST* image of the central part of the Orion Nebula combined with Wide Field Planetary Camera 2 images in different filters (O'Dell & Wong 1996). The white square corresponds to the FOV of the PMAS and the separate close-up image at the right-hand side shows the rebinned Hα map presented in Paper I. Inside of this box, the black rectangle indicates the slit position and the area covered by the UVES spectrum analysed in this paper (1.5×2.5 arcsec^2).

Doi, O'Dell & Hartigan (2004) have found a radial velocity of -39 ± 2 km s^{-1}, in agreement with previous results by Meaburn (1986) and O'Dell, Wen & Hester (1991). O'Dell & Henney (2008) have determined a tangential velocity of 59 ± 8 km s^{-1}, which is in agreement with previous determinations by O'Dell & Doi (2003). O'Dell & Henney (2008) have calculated a spatial velocity of 89 km s^{-1} and an angle of the velocity vector of 48° with respect to the plane of the sky, similar to the values found by Henney et al. (2007). Imaging studies by O'Dell et al. (1997) with the *Hubble Space Telescope* (*HST*) of the HH objects in the Orion Nebula show an extended [O III] emission in HH 202 and a strong [O III] emission in HH 202-S. This fact, together with the closeness of HH 202 to the main ionization source of the Orion Nebula, θ^1 Ori C, indicates that the excitation of the ionized gas is dominated by photoionization in HH 202-S, though the observed radial velocities imply that some shocked gas can be mixed in the region (Cantó et al. 1980). Photoionization-dominated flows are a minority in the inventory of HH objects, which are typically excited by shocks. This kind of HH objects is also known as 'irradiated jets' (Reipurth et al. 1998), since they are excited by the ultraviolet (UV) radiation from nearby massive stars. Irradiated jets have been found in the Orion Nebula (e.g. Bally & Reipurth 2001; O'Dell et al. 1997; Bally et al. 2006), the Pelican Nebula (Bally & Reipurth 2003), the Carina Nebula (Smith, Bally & Brooks 2004), NGC 1333 (Bally et al. 2006) and the Trifid Nebula (Cernicharo et al. 1998; Reipurth et al. 1998).

Mesa-Delgado, Esteban & García-Rojas (2008) have obtained the spatial distributions of the physical conditions and the ionic abundances in the Orion Nebula using long-slit spectroscopy at spatial scales of 1.2 arcsec. The goal of that work was to study the possible correlations between the local structures observed in the Orion Nebula – HH objects, proplyds, ionization fronts – and the abundance discrepancy (AD) that is found in H II regions. The AD is a classical problem in the study of ionized nebulae: the abundances of a given ion derived from recombination lines (RLs) are often between 0.1 and 0.3 dex higher than those obtained from collisionally excited lines (CELs) in H II regions (see García-Rojas & Esteban 2007; Esteban et al. 2004; Tsamis et al. 2003). The difference between those independent determinations of the abundance defines the AD factor (ADF). The predictions of the temperature fluctuation paradigm proposed by Peimbert (1967) – and parametrized by the mean square of the spatial distribution of temperature, the t^2 parameter – seem to account for the discrepancies observed in H II regions (see García-Rojas & Esteban 2007). A striking result found in the spatially resolved study of Mesa-Delgado et al. (2008) is that the ADF of O^{2+}, ADF(O^{2+}), shows larger values at the locations of HH objects as is the case of HH 202. Using integral-field spectroscopy with intermediate spectral resolution and a spatial resolution of 1×1 arcsec^2, Mesa-Delgado et al. (2009, hereafter Paper I) have mapped the emission line fluxes, the physical properties and the O^{2+} abundances derived from RLs and CELs of HH 202. They have found extended [O III] emission and higher values of the electron density and temperature as well as an enhanced ADF(O^{2+}) in HH 202-S, confirming the earlier results of Mesa-Delgado et al. (2008).

HH 529 is another HH object that is photoionized by θ^1 Ori C and shows similar characteristics to those of HH 202. Blagrave, Martin & Baldwin (2006) have performed deep optical echelle spectroscopy of that object with a 4 m class telescope and have detected and measured about 280 emission lines. Their high spectral resolution spectroscopy allowed them to separate the kinematic components associated with the ambient gas and with the flow. They have determined the physical conditions and the ionic abundances of oxygen from CELs and RLs in both components. However, they do not find high ADF(O^{2+}) and t^2 values in neither component. Another interesting result of Blagrave et al. (2006) is that the ionization structure of HH 529 indicates that it is a matter-bounded shock.

Motivated by the results found by Mesa-Delgado et al. (2008), inspired by the work of Blagrave et al. (2006) and in order to complement the results presented in Paper I, we have isolated the emission of the flow of HH 202-S knot using high spectral resolution spectroscopy, presenting the first complete physical and chemical analysis of this knot.

In Section 2, we describe the observations of HH 202 and the reduction procedure. In Section 3, we describe the emission line measurements, identifications and the reddening correction, we also compare our reddening determinations with those available in the literature. In Section 4, we describe the determinations of the physical conditions, the chemical – ionic and total – abundances and the ADF for O^+ and O^{2+}. In Section 5, we discuss (i) some inconsistencies found in the Balmer decrement of the lines of higher principal quantum number, (ii) the ionization structure of HH 202-S, (iii) the radial velocity pattern of the lines of each kinematic component, (iv) the t^2 parameter obtained from different methods and its possible relation with the ADF and (v) the evidences of dust grain

destruction in HH 202-S. Finally, in Section 6 we summarize our main conclusions.

2 OBSERVATIONS AND DATA REDUCTION

HH 202 was observed on 2003 March 30 at Cerro Paranal Observatory, Chile, using the UT2 (Kueyen) of the Very Large Telescope (VLT) with the Ultraviolet Visual Echelle Spectrograph (UVES; D'Odorico et al. 2000). The standard settings of UVES were used covering the spectral range from 3100 to 10 400 Å. Some narrow spectral ranges could not be observed. These are: 5783–5830 and 8540–8650 Å, due to the physical separation between the CCDs of the detector system of the red arm and 10 084–10 088 and 10 252–10 259 Å, because the last two orders of the spectrum do not fit completely within the size of the CCD. Five individual exposures of 90 s – for the 3100–3900 and 4750–6800 Å ranges – and 270 s – for the 3800–5000 and 6700–10 400 Å ranges – were added to obtain the final spectra. In addition, exposures of 5 and 10 s were taken to obtain good flux measurements – i.e. non-saturated – for the brightest emission lines. The spectral resolution was $\lambda/\Delta\lambda \approx 30\,000$. This high spectral resolution enables us to separate two kinematic components: one corresponding to the ambient gas – which we will call *nebular component* and whose emission mainly arises from behind HH 202 and, therefore, could not entirely correspond to the pre-shock gas – and another one corresponding to the gas flow of the HH object, the post-shock gas, which we will call *shock component*.

The slit was oriented north–south, and the atmospheric dispersion corrector (ADC) was used to keep the same observed region within the slit regardless of the airmass value. The HH object was observed between airmass values of 1.20 and 1.35. The average seeing during the observation was 0.7 arcsec. The slit width was set to 1.5 arcsec as a compromise between the spectral resolution needed and the desired signal-to-noise ratio of the spectra. The slit length was fixed to 10 arcsec. The one-dimensional spectra were extracted for an area of 1.5×2.5 arcsec^2. This area covers the apex of HH 202, the so-called knot HH 202-S, as we can see in Fig. 1. This zone shows the maximum shift in velocity between the shock and nebular components (see Fig. 2) allowing us to appropriately separate and study the spectra of both kinematic components.

The spectra were reduced using the IRAF[1] echelle reduction package, following the standard procedure of bias subtraction, aperture extraction, flat-fielding, wavelength calibration and flux calibration. The standard stars EG 247, C-32 9927 (Hamuy et al. 1992, 1994) and HD 49798 (Turnshek et al. 1990; Bohlin & Lindler 1992) were observed to perform the flux calibration. The error of the absolute flux calibration was of the order of 3 per cent.

3 LINE MEASUREMENTS, IDENTIFICATIONS AND REDDENING CORRECTION

Line fluxes were measured applying a double Gaussian profile fit procedure over the local continuum. All these measurements were made with the SPLOT routine of IRAF.

All line fluxes of a given spectrum have been normalized to a particular bright emission line present in the common range of two consecutive spectra. For the bluest spectrum (3100–3900 Å), the reference line was H9 3835 Å. For the range from 3800 to 5000 Å, the reference line was Hβ. In the case of the spectrum covering 4750–6800 Å, the reference was [O III] 4959 Å. Finally, for the reddest spectrum (6700–10 400 Å), the reference line was [S II] 6731 Å. In order to produce a final homogeneous set of line flux ratios, all of them were rescaled to the Hβ flux. In the case of the bluest spectra, the ratios were rescaled by the H9/Hβ ratio obtained from the 3800–5000 Å range. The emission line ratios of the 4750–6800 Å range were multiplied by the [O III] 4959/Hβ ratio measured in the 3800–5000 Å range. In the case of the last spectral section, 6700–10 400 Å, the rescaling factor was the [S II] 6731/Hβ ratio obtained from the 4750–6800 Å spectrum. All rescaling factors were measured in the short exposure spectra in order to avoid the possible saturation of the brightest emission lines. This process was done separately for both the nebular and shock components.

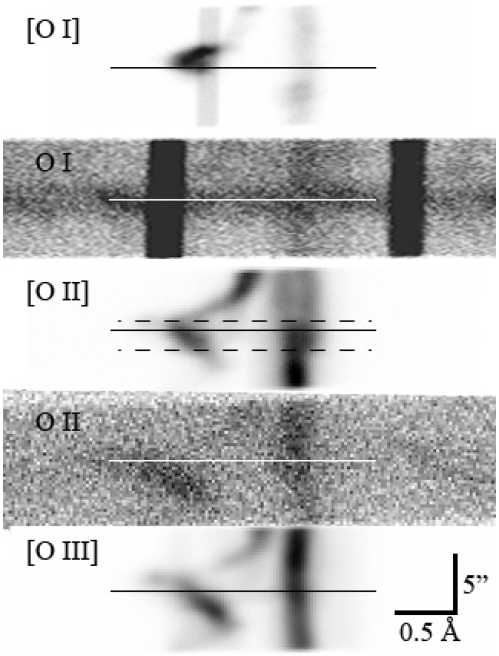

Figure 2. Sections of the bidimensional UVES spectrum showing the spatio-kinematic profiles of different oxygen lines: [O I] 6300 Å, O I 7772 Å, [O II] 3728 Å, O II 4649 Å and [O III] 4959 Å. Wavelength increases to the right and north points up. The solid straight lines in all the sections correspond to the slit centre and the dashed lines – only represented in the case of the [O II] 3728 Å profile – correspond to the extracted area 2.5 arcsec wide.

The spectral ranges present overlapping regions at the edges. The adopted flux of a line in the overlapping region was obtained as the average of the values obtained in both spectra. A similar procedure was considered in the case of lines present in two consecutive spectral orders of the same spectral range. The average of both measurements was considered for the adopted value of the line flux. In all cases, the differences in the line flux measured for the same line in different orders and/or spectral ranges do not show systematic trends and are always within the uncertainties.

The identification and laboratory wavelengths of the lines were obtained following a previous work on the Orion Nebula by Esteban et al. (2004), the compilations by Moore (1945) and the Atomic Line List v2.04.[2] The identification process and the measurement of line

[1] IRAF is distributed by National Optical Astronomy Observatories, which is operated by AURA (Association of Universities for Research in Astronomy), under cooperative agreement with NSF (National Science Foundation).

[2] Webpage at http://www.pa.uky.edu/~peter/atomic/.

fluxes were done simultaneously. The inspection of the line shapes at the bidimensional echelle spectrum was always used to identify which component – nebular or shock – was measured at each moment. The rather different spatial and spatio-kinematic structure of the two kinematic components is illustrated in Fig. 2. We have identified 360 emission lines in the spectrum of HH 202-S, 115 of them only show one component – eight belong to the nebular component and 107 belong to the shock one – and eight are dubious identifications.

For a given line, the observed wavelength is determined by the centroid of the Gaussian fit to the line profile. For lines measured in different orders and/or spectral ranges, the average of the different wavelength determinations has been adopted. From the adopted wavelength, the heliocentric velocity, $V_{\rm hel}$, has been calculated using the heliocentric correction appropriate for the coordinates of the object and the moment of observation. The typical error in the heliocentric velocity measured is about 1–2 km s^{-1}.

All line fluxes with respect to Hβ, $F(\lambda)/F(\mathrm{H}\beta)$, were dereddened using the typical relation,

$$\frac{I(\lambda)}{I(\mathrm{H}\beta)} = \frac{F(\lambda)}{F(\mathrm{H}\beta)} 10^{c(\mathrm{H}\beta) f(\lambda)}. \quad (1)$$

The reddening coefficient, $c(\mathrm{H}\beta)$, represents the amount of interstellar extinction which is the logarithmic extinction at Hβ, while $f(\lambda)$ is the adopted extinction curve normalized to $f(\mathrm{H}\beta) = 0$. The reddening coefficient was determined from the comparison of the observed flux ratio of Balmer and Paschen lines – those not contaminated by telluric or other nebular emissions – with respect to Hβ and the theoretical ones computed by Storey & Hummer (1995) for the physical conditions of $T_{\rm e} = 10\,000$ K and $n_{\rm e} = 1000\,{\rm cm}^{-3}$. As in Paper I, we have used the reddening function, $f(\lambda)$, normalized to Hβ derived by Blagrave et al. (2007) for the Orion Nebula. The use of this extinction law instead of the classical one (Costero & Peimbert 1970) produces slightly higher c(Hβ) values and also slightly different dereddened line fluxes depending on the spectral range (see Paper I). The final c(Hβ) values obtained for the two kinematic components were weighted averages of the values obtained for the individual lines: $c(\mathrm{H}\beta)_{\rm neb} = 0.41 \pm 0.02$ and $c(\mathrm{H}\beta)_{\rm sh} = 0.45 \pm 0.02$. Although not all the $c(\mathrm{H}\beta)$ values are consistent with each other (see Section 5.1), the average values obtained are quite similar and consistent within the uncertainties.

We can compare the reddening values with those obtained from integral-field spectroscopy data presented in Paper I in the same area of HH 202-S (see Fig. 1) and corresponding to the section $\Delta\alpha = [-4, -6]$ and $\Delta\delta = [-8, -5]$ (see fig. 3 of Paper I). The average $c(\mathrm{H}\beta)$ in this zone is 0.65 ± 0.15, which is higher than those determined for UVES data. However, if we recalculate the value of $c(\mathrm{H}\beta)$ from the UVES data using the same Balmer lines as in Paper I, we obtain a value 0.5 ± 0.1 in both kinematic components, a value consistent with the Potsdam Multi-Aperture Spectrograph (PMAS) one within the errors. These differences can be related to several systematical disagreements found between the $c(\mathrm{H}\beta)$ values obtained from different individual Balmer or Paschen lines (see Section 5.1).

In the most complete work on the reddening distribution across the Orion Nebula, O'Dell & Yusef-Zadeh (2000) obtain values of $c(\mathrm{H}\beta)$ between 0.2 and 0.4 in the zone around HH 202-S, somewhat lower than our reddening determinations. This can be due to the fact that O'Dell & Yusef-Zadeh use the extinction law by Costero & Peimbert (1970) which, as we discuss in Paper I, produces lower $c(\mathrm{H}\beta)$ values than the more recent extinction law (Blagrave et al. 2007). We have also recalculated $c(\mathrm{H}\beta)$ from our UVES spectra making use of the Costero & Peimbert law, and we obtain values about 0.3, being now in agreement with the determinations of O'Dell & Yusef-Zadeh (2000).

In Table 1, the final list of line identifications (Columns 1–3), $f(\lambda)$ values (Column 4), heliocentric velocities (Columns 5 and 8) and dereddened flux line ratios (Columns 6 and 9) for the nebular and shock components are presented. The observational errors associated with the line dereddened fluxes with respect to Hβ – in percentage – are also presented in Columns (7) and (10) of Table 1. These errors include the uncertainties in line flux measurement, flux calibration and error propagation in the reddening coefficient.

In Column (11) of Table 1, we present the shock-to-nebular line flux ratio for those lines in which both kinematic components have been measured. This ratio is defined as

$$\frac{I_{\rm sh}}{I_{\rm neb}} = \frac{[I(\lambda)/I(\mathrm{H}\beta)]_{\rm sh}}{[I(\lambda)/I(\mathrm{H}\beta)]_{\rm neb}} = \frac{I(\lambda)_{\rm sh}}{I(\lambda)_{\rm neb}} \times \frac{I(\mathrm{H}\beta)_{\rm neb}}{I(\mathrm{H}\beta)_{\rm sh}}, \quad (2)$$

where the integrated dereddened Hβ fluxes are $I(\mathrm{H}\beta)_{\rm neb} = (3.80 \pm 0.20) \times 10^{-12}$ and $I(\mathrm{H}\beta)_{\rm sh} = (6.00 \pm 0.20) \times 10^{-12}$ erg cm^{-2} s^{-1}. The $I_{\rm neb}/I_{\rm sh}$ ratios depend on each particular line. In general, they are close to 1 for H I lines but become less than 1 for higher ionized species – except Fe ions – and are typically greater than 1 for neutral species. A more extensive discussion on this particular issue will be presented in Section 5.2.

In Fig. 3, we show a section of our flux-calibrated echelle spectra around the lines of multiplet 1 of O II. It can be seen that both the nebular and the shock components are well separated and show a remarkable high signal-to-noise ratio.

4 RESULTS

4.1 Excitation mechanism of the ionized gas in HH 202-S

In their recent work, O'Dell & Henney (2008) argue that the presence of a variety of ionization stages in the ionized gas of HH 202 indicates that the flow also contains neutral material. They interpret that fact as due to the impact of the flow with pre-existing neutral material – perhaps of the foreground veil – or that the flow compresses the ambient ionized gas inside the nebula to such degree that it traps the ionization front. Our results provide some clues that can help to ascertain this issue. The value of some emission line ratios are good indicators of the presence of shock excitation in ionized gas, especially [S II]/Hα and [O I]/Hα. In our spectra, we find log([S II] 6717+31/Hα) values which are almost identical in both kinematic components (-1.49 and -1.44 for the nebular and shock components, respectively). These values are completely consistent with those expected for photoionized nebulae and far from the range of values between -0.5 and 0.5, which is the typical of supernova remnants and HH objects (see fig. 10 of Riera et al. 1989). On the other hand, the values of log([O I] 6300/Hα) that we obtain for the nebular and shock components are of -2.66 and -2.22, somewhat different in this case, but also far from the values expected in the case of substantial contribution of shock excitation (Hartigan, Raymond & Hartmann 1987). Finally, we have also used the diagnostic diagrams of Raga et al. (2008) where the [N II] 6548/Hα and [S II] 6717+31/Hα versus [O III] 5007/Hα ratios of HH 202 are found in the zone dominated by photoionized shocks. Therefore, the spectrum of HH 202-S seems to be consistent with the picture that the bulk of the emission in this area is produced by photoionization acting on compressed ambient gas that has trapped the ionization front inside the ionized bubble of the nebula. In the rest of the

Table 1. Identifications, reddening-corrected line ratios [$I(\mathrm{H}\beta) = 100$] for an area of 1.5×2.5 arcsec^2 and heliocentric velocities for the nebular and shock components.

				Nebular component			Shock component				
λ_0 (Å)[a]	Ion[a]	Mult[a]	$f(\lambda)$[b]	$V_{\rm hel}$[c]	$I(\lambda)$[d]	Error (per cent)[e]	$V_{\rm hel}$[c]	$I(\lambda)$[d]	Error (per cent)[e]	$I_{\rm sh}/I_{\rm neb}$[f]	Notes
3187.74	He I	3	0.195	15	3.450	6	-34	3.682	6	1.067	
3239.74	[Fe III]	6F	0.194	–	–	–	−35	0.806	15	–	
3286.19	[Fe III]	6F	0.192	–	–	–	−35	0.206	15	–	
3319.21	[Fe III]	6F	0.191	–	–	–	−38	0.114	40	–	
3322.54	[Fe III]	5F	0.191	–	–	–	−48	0.744	9	–	
3334.90	[Fe III]	6F	0.190	–	–	–	−36	0.320	9	–	
3354.55	He I	8	0.189	14	0.148	10	−33	0.159	10	1.079	
3355.49	[Fe III]	6F	0.189	–	–	–	−37	0.189	10	–	
3356.57	[Fe III]	6F	0.189	–	–	–	−35	0.262	9	–	
3366.20	[Fe III]	6F	0.189	–	–	–	−35	0.119	40	–	
3371.41	[Fe III]	5F	0.188	–	–	–	−47	0.543	11	–	
3406.18	[Fe III]	5F	0.186	–	–	–	−48	0.250	11	–	
3447.59	He I	7	0.184	16	0.241	9	−34	0.246	9	1.019	
3498.66	He I	40	0.180	10	0.090	15	−36	0.054	18	0.595	
3512.52	He I	38	0.179	13	0.195	10	−38	0.176	10	0.901	
3530.50	He I	36	0.178	12	0.129	10	−34	0.147	10	1.136	
3554.42	He I	34	0.176	15	0.224	10	−36	0.219	10	0.976	
3587.28	He I	32	0.173	13	0.331	9	−36	0.339	9	1.024	
3613.64	He I	6	0.171	15	0.435	9	−37	0.462	9	1.061	
3634.25	He I	28	0.169	13	0.425	9	−35	0.464	9	1.090	
3664.68	H I	H28	0.166	13	0.172	10	−36	0.251	9	1.457	
3666.10	H I	H27	0.166	13	0.355	9	−36	0.347	9	0.977	
3667.68	H I	H26	0.166	13	0.414	9	−36	0.458	9	1.105	
3669.47	H I	H25	0.166	13	0.468	9	−36	0.502	9	1.072	
3671.48	H I	H24	0.165	13	0.543	9	−36	0.586	9	1.079	
3673.76	H I	H23	0.165	14	0.557	9	−36	0.645	9	1.157	
3676.37	H I	H22	0.165	15	0.661	9	−36	0.721	9	1.091	
3679.36	H I	H21	0.165	15	0.761	9	−36	0.841	9	1.105	
3682.81	H I	H20	0.164	14	0.822	9	−36	0.887	9	1.079	
3686.83	H I	H19	0.164	15	0.867	9	−36	0.993	9	1.146	
3691.56	H I	H18	0.163	14	1.106	9	−37	1.148	9	1.038	
3697.15	H I	H17	0.163	14	1.271	6	−36	1.312	6	1.032	
3703.86	H I	H16	0.162	13	1.409	6	−37	1.502	6	1.065	
3705.04	He I	25	0.162	10	0.646	9	−39	0.717	9	1.108	
3711.97	H I	H15	0.161	14	1.745	6	−36	1.834	6	1.050	
3721.83	[S III]	2F	0.160	10	4.041	6	−39	3.363	6	0.832	
3721.93	H I	H14									
3726.03	[O II]	1F	0.160	22	87.30	5	−34	70.12	5	0.803	
3728.82	[O II]	1F	0.160	18	52.04	5	−36	28.15	5	0.540	
3734.37	H I	H13	0.159	13	2.542	6	−36	2.581	6	1.015	
3750.15	H I	H12	0.158	14	3.081	6	−36	3.143	6	1.020	
3770.63	H I	H11	0.155	14	3.967	6	−36	4.087	6	1.030	
3797.63	[S III]	2F	0.152	35	5.240	5	−15	5.381	5	1.027	
3797.90	H I	H10									
3805.74	He I	58	0.152	12	0.063	15	−37	0.045	18	0.720	
3819.61	He I	22	0.150	14	1.129	9	−35	1.153	7	1.020	
3833.57	He I	62	0.149	14	0.067	15	−39	0.077	15	1.158	
3835.39	H I	H9	0.148	13	7.271	6	−37	7.242	6	0.996	
3856.02	Si II	1	0.146	16	0.211	10	−38	0.309	10	1.469	
3862.59	Si II	1	0.145	16	0.120	12	−38	0.175	12	1.450	
3868.75	[Ne III]	1F	0.145	12	12.94	5	−34	8.096	6	0.625	
3871.82	He I	60	0.144	10	0.084	15	−39	0.087	15	1.034	
3888.65	He I	2	0.142	16	6.717	6	−39	5.625	6	0.837	
3889.05	H I	H8	0.142	13	11.52	4	−45	9.043	6	0.784	
3918.98	C II	4	0.139	9	0.049	18	−39	0.062	18	1.267	
3920.68	C II	4	0.139	9	0.098	15	−39	0.106	15	1.086	
3926.53	He I	58	0.138	15	0.122	10	−36	0.135	10	1.102	
3964.73	He I	5	0.133	13	0.906	9	−36	0.937	9	1.034	
3967.46	[Ne III]	1F	0.133	13	3.866	6	−36	2.574	6	0.665	
3970.07	H I	H7	0.133	13	15.68	4	−37	15.93	4	1.016	
3993.06	[Ni II]	4F	0.130	28	0.033	20	−40	0.041	18	1.227	
4008.36	[Fe III]	4F	0.128	–	–	–	−42	0.587	9	–	*g*

Table 1 – *continued*

				Nebular component			Shock component				
λ_0 (Å)[a]	Ion[a]	Mult[a]	$f(\lambda)$[b]	V_{hel}[c]	$I(\lambda)$[d]	Error (per cent)[e]	V_{hel}[c]	$I(\lambda)$[d]	Error (per cent)[e]	I_{sh}/I_{neb}[f]	Notes
4009.22	He I	55	0.128	16	0.170	10	−35	0.222	10	1.312	*g*
4023.98	He I	54	0.126	16	0.028	20	−39	0.026	20	0.935	
4026.08	N II	40	0.126	13	2.195	6	−37	2.110	6	0.961	
4026.21	He I	18									
4046.43	[Fe III]	4F	0.123	–	–	–	−38	0.084	15	–	
4068.60	[S II]	1F	0.121	23	0.887	9	−35	5.318	6	5.996	
4069.62	O II	10	0.121	25	0.288	10	−28	0.197	15	0.683	*g*
4069.89	O II	10									
4072.15	O II	10	0.120	15	0.066	15	−38	0.045	18	0.683	
4076.35	[S II]	1F	0.120	23	0.362	9	−35	1.800	6	4.968	
4079.70	[Fe III]	4F	0.119	–	–	–	−42	0.154	10	–	
4089.29	O II	48	0.118	13	0.012	30	−38	0.021	28	1.754	
4092.93	O II	10	0.118	11	0.014	30	−34	0.008	35	0.595	
4096.61	[Fe III]	4F	0.117	9	0.028	40	−37	0.036	20	1.295	
4097.22	O II	20	0.117	15	0.025	25	−34	0.020	40	0.789	
4097.26	O II	48									
4101.74	H I	H6	0.117	14	24.75	4	−37	25.10	4	1.014	
4114.48	[Fe II]	23F	0.115	–	–	–	−42	0.083	15	–	
4119.22	O II	20	0.114	12	0.014	30	−40	0.019	28	1.355	
4120.82	He I	16	0.114	12	0.175	10	−35	0.199	10	1.134	*g*
4121.46	O II	19	0.114	7	0.031	20	−34	0.047	18	1.511	*g*
4132.80	O II	19	0.113	9	0.027	20	−45	0.051	18	1.881	
4143.76	He I	53	0.111	13	0.281	9	−37	0.304	9	1.082	
4153.30	O II	19	0.110	10	0.037	18	−42	0.042	18	1.141	
4156.36	N II	19	0.110	14	0.034	18	−37	0.030	20	0.896	*h*
4168.97	He I	52	0.108	18	0.052	18	−34	0.055	18	1.044	
4177.20	[Fe II]	21F	0.107	26	0.015	40	−41	0.041	20	2.695	
4178.96	[Fe II]	23F	0.107	–	–	–	−42	0.023	30	–	
4185.45	O II	36	0.106	11	0.026	20	−36	0.009	35	0.363	
4189.79	O II	36	0.105	10	0.024	20	−51	0.023	20	0.939	
4201.17	[Ni II]	4F	0.104	–	–	–	−40	0.015	30	–	
4211.10	[Fe II]	23F	0.103	–	–	–	−40	0.034	18	–	
4243.97	[Fe II]	21F	0.098	22	0.104	10	−41	0.275	9	2.649	
4251.44	[Fe II]	23F	0.097	–	–	–	−41	0.018	40	–	
4267.15	C II	6	0.095	15	0.247	9	−35	0.211	10	0.854	
4276.83	[Fe II]	21F	0.094	26	0.039	18	−40	0.147	10	3.776	
4287.39	[Fe II]	7F	0.093	27	0.083	15	−41	0.280	9	3.379	
4303.82	O II	53	0.091	10	0.027	20	−34	0.016	30	0.574	
4317.14	O II	2	0.089	9	0.021	28	−49	0.045	18	2.174	
4319.62	[Fe II]	21F	0.088	–	–	–	−41	0.077	15	–	
4326.24	[Ni II]	^{2}D-^{4}P	0.088	28	0.041	18	−28	0.311	:	7.603	
4340.47	H I	Hγ	0.086	13	46.21	4	−37	46.56	4	1.007	
4345.55	O II	63.01	0.085	11	0.035	18	−42	0.069	15	1.958	
4346.85	[Fe II]	21F	0.085	–	–	–	−41	0.056	18	–	
4349.43	O II	2	0.084	11	0.047	18	−37	0.051	18	1.088	
4352.78	[Fe II]	21F	0.084	26	0.027	40	−41	0.071	18	2.647	
4358.36	[Fe II]	21F	0.083	–	–	–	−41	0.046	15	–	
4359.34	[Fe II]	7F	0.083	26	0.060	15	−41	0.209	10	3.488	
4363.21	[O III]	2F	0.082	13	0.944	9	−36	0.934	9	0.989	
4366.89	O II	2	0.081	10	0.025	20	−41	0.046	18	1.843	
4368.19	O I	5	0.081	29	0.082	15	−29	0.030	20	0.361	
4368.25	O I	5									
4372.43	[Fe II]	21F	0.081	–	–	–	−41	0.032	20	–	
4387.93	He I	51	0.078	14	0.523	9	−37	0.563	9	1.076	
4413.78	[Fe II]	7F	0.073	28	0.055	15	−41	0.151	10	2.766	*g*
4414.90	O II	5	0.073	15	0.037	20	−32	0.024	20	0.638	*g*
4416.27	[Fe II]	6F	0.073	23	0.054	15	−41	0.237	9	4.412	*g*
4416.97	O II	5	0.073	13	0.021	28	−33	0.343	20	16.53	*g*
4432.45	[Fe II]	6F	0.070	–	–	–	−41	0.020	28	–	
4437.55	He I	50	0.069	14	0.063	15	−36	0.071	15	1.121	
4452.11	[Fe II]	7F	0.067	26	0.034	18	−42	0.095	15	2.764	
4452.38	O II	5									
4457.95	[Fe II]	6F	0.066	27	0.022	20	−42	0.102	10	4.599	

Table 1 – *continued*

				Nebular component			Shock component				
λ_0 (Å)[a]	Ion[a]	Mult[a]	$f(\lambda)$[b]	V_{hel}[c]	$I(\lambda)$[d]	Error (per cent)[e]	V_{hel}[c]	$I(\lambda)$[d]	Error (per cent)[e]	I_{sh}/I_{neb}[f]	Notes
4471.47	He I	14	0.064	15	4.303	6	−35	4.405	6	1.023	
4474.91	[Fe II]	7F	0.063	25	0.012	:	−42	0.044	18	3.655	
4488.75	[Fe II]	6F	0.061	–	–	–	−42	0.033	20	–	
4492.64	[Fe II]	6F	0.060	26	0.011	:	−41	0.032	20	3.025	
4509.60	[Fe II]	6F	0.057	–	–	–	−38	0.011	:	–	*h*
4514.90	[Fe II]	6F	0.056	–	–	–	−41	0.024	40	–	*h*
4528.38	[Fe II]	6F	0.054	–	–	–	−42	0.010	:	–	*h*
4563.18	[Cr III]?		0.048	–	–	–	−78	0.020	40	–	
4571.10	Mg I]	1	0.047	10	0.034	30	−41	0.215	9	6.377	
4581.14	[Cr II]?		0.045	–	–	–	−49	0.024	30	–	
4590.97	O II	15	0.044	14	0.016	40	−36	0.017	40	1.071	
4597.00	[Co IV]?		0.043	–	–	–	−39	0.122	10	–	
4601.48	N II	5	0.042	14	0.027	40	−42	0.020	40	0.753	
4607.13	[Fe III]	3F	0.041	13	0.065	15	−43	0.752	9	11.51	
4607.16	N II	5									
4628.05	[Ni II]	^{2}D-^{4}P	0.037	29	0.008	:	−39	0.014	40	1.685	
4630.54	N II	5	0.037	13	0.035	18	−37	0.041	18	1.178	
4638.86	O II	1	0.036	10	0.065	15	−41	0.044	18	0.678	
4641.81	O II	1	0.035	12	0.072	15	−39	0.077	15	1.065	
4641.85	N III	2									
4649.13	O II	1	0.034	13	0.102	10	−38	0.093	15	0.908	
4650.84	O II	1	0.034	15	0.049	18	−43	0.045	18	0.929	
4658.10	[Fe III]	3F	0.032	18	0.870	9	−39	10.98	5	12.62	
4661.63	O II	1	0.032	11	0.048	18	−38	0.059	15	1.207	
4667.01	[Fe III]	3F	0.031	9	0.047	30	−40	0.531	9	11.42	
4673.73	O II	1	0.030	13	0.008	35	−38	0.006	40	0.738	
4676.24	O II	1	0.030	11	0.024	20	−38	0.026	20	1.106	
4701.62	[Fe III]	3F	0.025	14	0.237	9	−43	3.915	6	16.52	
4711.37	[Ar IV]	1F	0.024	12	0.014	40	–	–	–	–	
4713.14	He I	12	0.023	15	0.570	9	−35	0.551	9	0.966	
4728.07	[Fe II]	4F	0.021	–	–	–	−41	0.054	15	–	
4733.93	[Fe III]	3F	0.020	14	0.125	10	−42	1.842	6	14.77	
4740.16	[Ar IV]	1F	0.019	15	0.016	40	–	–	–	–	
4754.83	[Fe III]	3F	0.017	13	0.167	10	−46	2.070	6	12.39	
4769.60	[Fe III]	3F	0.014	7	0.098	10	−48	1.391	6	14.21	
4774.74	[Fe II]	20F	0.014	24	0.007	:	−42	0.044	18	6.607	
4777.88	[Fe III]	3F	0.013	7	0.036	25	−51	0.901	9	24.92	
4814.55	[Fe II]	20F	0.007	26	0.071	15	−41	0.211	10	2.947	
4861.33	H I	Hβ	0.000	14	100.0	4	−37	100.0	4	1.000	
4874.48	[Fe II]	20F	−0.002	–	–	–	−41	0.039	18	–	
4881.00	[Fe III]	2F	−0.003	20	0.342	9	−38	5.776	6	16.86	
4889.70	[Fe II]	3F	−0.005	23	0.074	18	−45	0.159	10	2.171	
4902.65	Si II	7.23	−0.007	10	0.016	:	−39	0.010	30	0.642	*g*
4905.34	[Fe II]	20F	−0.007	19	0.031	:	−40	0.071	20	2.311	*g*
4921.93	He I	48	−0.010	13	1.195	6	−37	1.181	6	0.988	
4924.50	[Fe III]	2F	−0.010	21	0.063	20	−37	0.074	15	1.221	
4924.53	O II	28									
4930.50	[Fe III]	1F	−0.011	25	0.195	15	−32	0.527	9	2.706	*g*
4931.32	[O III]	1F	−0.011	11	0.038	22	−38	0.027	20	0.702	*g*
4947.38	[Fe II]	20F	−0.013	23	0.016	35	−39	0.031	20	2.309	
4950.74	[Fe II]	20F	−0.014	–	–	–	−40	0.030	19	–	
4958.91	[O III]	1F	−0.015	13	101.9	5	−35	71.55	5	0.702	
4973.39	[Fe II]	20F	−0.017	–	–	–	−41	0.029	20	–	
4985.90	[Fe III]	2F	−0.019	–	–	–	−44	0.045	40	–	
4987.20	[Fe III]	2F	−0.019	22	0.097	30	−38	1.069	6	11.07	
4987.38	N II	24									
5006.84	[O III]	1F	−0.022	13	303.8	5	−35	213.5	5	0.702	
5011.30	[Fe III]	1F	−0.023	18	0.182	15	−40	1.968	6	10.80	
5015.68	He I	4	−0.024	13	2.357	6	−37	2.396	6	1.016	
5020.23	[Fe II]	20F	−0.024	–	–	–	−39	0.035	25	–	
5041.03	Si II	5	−0.028	15	0.178	10	−37	0.141	10	0.792	
5043.52	[Fe II]	20F	−0.028	–	–	–	−40	0.020	:	–	
5047.74	He I	47	−0.028	–	–	–	−37	0.148	10	–	*g*

Table 1 – *continued*

				Nebular component			Shock component				
λ_0 (Å)[a]	Ion[a]	Mult[a]	$f(\lambda)$[b]	V_{hel}[c]	$I(\lambda)$[d]	Error (per cent)[e]	V_{hel}[c]	$I(\lambda)$[d]	Error (per cent)[e]	I_{sh}/I_{neb}[f]	Notes
5055.98	Si II	5	−0.030	17	0.224	9	−36	0.274	9	1.223	
5084.77	[Fe III]	1F	−0.034	–	–	–	−40	0.332	9	–	
5111.63	[Fe II]	19F	−0.038	–	–	–	−41	0.103	10	–	
5146.61	O I	28	−0.043	28	0.041	18	–	–	–	–	
5146.65	O I	28									
5158.00	[Fe II]	18F	−0.045	–	–	–	−41	0.061	15	–	*g*
5158.81	[Fe II]	19F	−0.045	25	0.077	15	−42	0.722	9	9.373	*g*
5163.95	[Fe II]	35F	−0.045	–	–	–	−40	0.044	18	–	
5181.95	[Fe II]	18F	−0.048	–	–	–	−39	0.023	25	–	
5191.82	[Ar III]	3F	−0.049	6	0.045	20	−41	0.059	20	1.303	
5197.90	[N I]	1F	−0.050	28	0.224	9	−32	0.037	18	0.164	*i*
5200.26	[N I]	1F	−0.051	28	0.111	10	−33	0.010	30	0.091	*i*
5220.06	[Fe II]	19F	−0.053	–	–	–	−40	0.073	18	–	
5261.61	[Fe II]	19F	−0.059	28	0.052	15	−40	0.318	9	6.083	
5268.88	[Fe II]	18F	−0.060	–	–	–	−40	0.022	20	–	
5270.40	[Fe III]	1F	−0.060	24	0.418	9	−33	6.378	6	15.24	
5273.38	[Fe II]	18F	−0.061	25	0.037	18	−42	0.160	10	4.374	
5296.83	[Fe II]	19F	−0.064	–	–	–	−41	0.032	25	–	
5298.89	O I	26	−0.064	25	0.030	30	–	–	–	–	
5299.04	O I	26									
5333.65	[Fe II]	19F	−0.069	23	0.028	40	−41	0.165	10	5.827	
5376.45	[Fe II]	19F	−0.075	–	–	–	−41	0.111	10	–	
5412.00	[Fe III]	1F	−0.080	23	0.054	40	−33	0.597	9	11.01	
5412.65	[Fe II]	17F	−0.080	–	–	–	−41	0.055	40	–	
5433.13	[Fe II]	18F	−0.082	–	–	–	−41	0.050	25	–	
5436.43	[Cr III]	2F	−0.083	–	–	–	−44	0.048	25	–	
5454.72	[Cr III]	2F	−0.085	–	–	–	−41	0.056	20	–	
5472.35	[Cr III]	2F	−0.088	–	–	–	−43	0.083	15	–	
5485.03	[Cr III]	2F	−0.089	–	–	–	−44	0.052	20	–	
5495.82	[Fe II]	17F	−0.091	–	–	–	−40	0.034	30	–	
5506.87	[Cr III]	2F	−0.092	–	–	–	−41	0.153	10	–	
5512.77	O I	25	−0.093	26	0.020	20	−42	0.012	30	0.618	
5517.71	[Cl III]	1F	−0.093	12	0.507	9	−36	0.271	9	0.535	
5527.34	[Fe II]	17F	−0.095	–	–	–	−41	0.173	10	–	
5537.88	[Cl III]	1F	−0.096	12	0.507	9	−39	0.555	9	1.095	
5551.96	[Cr III]	2F	−0.098	–	–	–	−45	0.278	9	–	
5554.83	O I	24	−0.098	34	0.041	18	–	–	–	–	
5555.03	O I	24									
5654.86	[Fe II]	17F	−0.111	–	–	–	−42	0.018	28	–	
5666.64	N II	3	−0.113	13	0.022	40	−37	0.017	40	0.765	
5679.56	N II	3	−0.114	13	0.024	40	−34	0.031	40	1.302	
5714.61	[Cr III]	1F	−0.119	–	–	–	−43	0.132	10	–	
5746.97	[Fe II]	34F	−0.123	–	–	–	−41	0.022	25	–	
5754.64	[N II]	3F	−0.124	21	0.646	9	−37	1.565	6	2.421	
5875.64	He I	11	−0.138	13	12.969	5	−37	13.024	5	1.004	
5885.88	[Cr III]	1F	−0.140	–	–	–	−45	0.106	18	–	
5887.67	[Mn II]?		−0.140	–	–	–	−32	0.039	25	–	*i*
5890.27	[Co II]	b^3P-c^3F	−0.140	–	–	–	−54	0.095	25	–	*i*
5931.78	N II	28	−0.145	25	0.027	18	−42	0.026	:	0.976	
5941.65	N II	28	−0.147	10	0.009	30	−39	0.024	:	2.554	
5957.56	Si II	4	−0.148	19	0.087	30	−39	0.102	15	1.177	
5958.39	O I	23	−0.149	31	0.037	:	–	–	–	–	
5958.58	O I	23									
5978.93	Si II	4	−0.151	19	0.129	15	−38	0.182	11	1.410	
5983.32	[Cr III]	1F	−0.152	–	–	–	−47	0.047	18	–	
5987.62	[Co II]	b^3P-c^3F	−0.152	–	–	–	−54	0.040	20	–	
6000.10	[Ni III]	2F	−0.154	–	–	–	−34	0.167	15	–	
6046.23	O I	22	−0.159	35	0.086	15	−27	0.023	25	0.268	
6046.44	O I	22									
6046.49	O I	22									
6300.30	[O I]	1F	−0.189	27	0.544	9	−32	1.691	6	3.106	*j*
6312.10	[S III]	3F	−0.191	14	1.700	6	−38	2.248	6	1.322	
6347.11	Si II	2	−0.195	18	0.194	12	−39	0.297	9	1.531	

Table 1 – *continued*

				Nebular component				Shock component			
λ_0 (Å)[a]	Ion[a]	Mult[a]	$f(\lambda)$[b]	V_{hel}[c]	$I(\lambda)$[d]	Error (per cent)[e]	V_{hel}[c]	$I(\lambda)$[d]	Error (per cent)[e]	I_{sh}/I_{neb}[f]	Notes
6363.78	[O I]	1F	−0.197	26	0.207	9	−32	0.554	9	2.676	*j*
6371.36	Si II	2	−0.198	15	0.107	15	−39	0.150	12	1.406	
6440.40	[Fe II]	15F	−0.206	–	–	–	−41	0.037	18	–	
6533.80	[Ni III]	2F	−0.217	–	–	–	−51	0.264	9	–	
6548.03	[N II]	1F	−0.218	24	15.60	5	−34	24.83	5	1.591	
6562.82	H I	Hα	−0.220	13	279.4	4	−38	283.1	4	1.013	
6576.30	[Co III]	a^4F-a^4P	−0.222	–	–	–	−48	0.049	20	–	
6578.05	C II	2	−0.222	13	0.196	12	−38	0.215	12	1.093	
6583.41	[N II]	1F	−0.223	24	46.67	5	−35	76.64	5	1.642	
6666.80	[Ni II]	8F	−0.232	–	–	–	−40	0.068	20	–	
6678.15	He I	46	−0.234	13	3.462	6	−37	3.532	6	1.020	
6682.20	[Ni III]	2F	−0.234	–	–	–	−53	0.085	15	–	
6716.47	[S II]	2F	−0.238	22	3.715	6	−36	3.211	6	0.864	
6730.85	[S II]	2F	−0.240	23	5.405	6	−36	7.041	6	1.302	
6739.80	[Fe IV]	–	−0.241	–	–	–	−37	0.015	30	–	
6747.50	[Cr IV]?	–	−0.242	–	–	–	−37	0.038	25	–	
6797.00	[Ni III]	2F	−0.247	–	–	–	−53	0.035	20	–	
6809.23	[Fe II]	31F	−0.249	–	–	–	−40	0.008	35	–	
6813.57	[Ni II]	8F	−0.249	–	–	–	−42	0.007	35	–	
6946.40	[Ni III]	2F	−0.265	–	–	–	−51	0.046	18	–	
6961.50	[Co III]	a^4F-a^4P	−0.266	–	–	–	−49	0.011	35	–	
7001.92	O I	21	−0.271	36	0.088	15	−25	0.053	15	0.603	*i*
7002.23	O I	21									
7035.30	[Co II]?	a^1D-c^3P	−0.275	–	–	–	−74	0.011	35	–	
7065.28	He I	10	−0.278	11	5.366	6	−40	4.677	6	0.871	
7078.10	[V II]?		−0.280	–	–	–	−33	0.010	40	–	
7088.30	[Cr III]?		−0.281	–	–	–	−33	0.026	30	–	
7125.74	[V II]?		−0.285	–	–	–	−63	0.009	30	–	
7135.78	[Ar III]	1F	−0.286	13	12.88	6	−37	14.46	6	1.122	
7152.70	[Co III]?	a^4F-a^4P	−0.288	–	–	–	−32	0.025	18	–	
7155.16	[Fe II]	14F	−0.289	25	0.057	15	−42	1.045	6	18.48	
7160.58	He I	1/10	−0.289	12	0.027	18	−38	0.023	18	0.847	
7172.00	[Fe II]	14F	−0.291	–	–	–	−43	0.286	9	–	
7231.34	C II	3	−0.297	12	0.081	15	−39	0.069	15	0.856	*i*
7236.42	C II	3	−0.298	12	0.164	12	−36	0.117	15	0.712	*i*
7254.15	O I	20	−0.300	34	0.133	11	−25	0.030	18	0.221	*i*
7254.45	O I	20									
7254.53	O I	20									
7281.35	He I	45	−0.303	14	0.594	9	−36	0.709	9	1.191	
7291.47	[Ca II]	1F	−0.304	–	–	–	−43	0.480	9	–	
7298.05	He I	1/9	−0.305	13	0.026	18	−39	0.024	18	0.918	*i*
7318.92	[O II]	2F	−0.307	28	0.880	6	−30	3.061	6	3.476	*g*, *i*
7319.99	[O II]	2F	−0.308	27	3.257	6	−32	10.19	5	3.129	*g*, *i*
7323.89	[Ca II]	1F	−0.308	–	–	–	−43	0.342	9	–	
7329.66	[O II]	2F	−0.309	23	1.589	6	−36	5.548	6	3.492	*g*, *i*
7330.73	[O II]	2F	−0.309	22	1.814	6	−36	5.502	6	3.032	*g*, *i*
7377.83	[Ni II]	2F	−0.314	29	0.070	11	−40	0.965	6	13.73	
7388.16	[Fe II]	14F	−0.315	–	–	–	−42	0.202	9	–	
7411.61	[Ni II]	2F	−0.318	28	0.026	18	−40	0.101	11	3.869	
7452.54	[Fe II]	14F	−0.323	25	0.021	20	−41	0.333	9	15.58	
7499.85	He I	1/8	−0.328	13	0.038	15	−37	0.038	15	0.990	
7637.54	[Fe II]	1F	−0.344	–	–	–	−43	0.120	20	–	
7686.94	[Fe II]	1F	−0.349	–	–	–	−43	0.108	18	–	
7751.10	[Ar III]	2F	−0.356	14	3.118	6	−37	3.488	6	1.118	*i*
7771.94	O I	1	−0.359	25	0.011	30	−42	0.012	28	1.115	*g*, *i*
7774.17	O I	1	−0.359	–	–	–	−43	0.026	18	–	*g*, *i*
7775.39	O I	1	−0.359	21	0.005	35	−42	0.006	35	1.115	*g*, *i*
7816.13	He I	1/7	−0.363	14	0.062	15	−37	0.051	15	0.830	
7889.90	[Ni III]	1F	−0.372	22	0.049	15	−35	0.736	6	15.13	
8000.08	[Cr II]	1F	−0.384	26	0.014	28	−43	0.053	15	3.704	
8125.30	[Cr II]	1F	−0.397	26	0.013	28	−41	0.045	15	3.383	
8260.93	H I	P36	−0.411	15	0.033	18	−37	0.046	15	1.400	
8264.28	H I	P35	−0.412	16	0.068	11	−34	0.064	11	0.936	

Table 1 – *continued*

				Nebular component			Shock component				
λ_0 (Å)[a]	Ion[a]	Mult[a]	$f(\lambda)$[b]	V_{hel}[c]	$I(\lambda)$[d]	Error (per cent)[e]	V_{hel}[c]	$I(\lambda)$[d]	Error (per cent)[e]	I_{sh}/I_{neb}[f]	Notes
8267.94	H I	P34	−0.412	15	0.053	15	−37	0.067	11	1.245	
8271.93	H I	P33	−0.413	14	0.067	11	−39	0.068	11	1.009	
8276.31	H I	P32	−0.413	14	0.076	11	−38	0.086	11	1.127	
8281.12	H I	P31	−0.414	23	0.057	15	−36	0.104	11	1.831	
8286.43	H I	P30	−0.414	10	0.075	11	−46	0.042	15	0.563	*i*
8292.31	H I	P29	−0.415	13	0.091	11	−37	0.111	11	1.221	
8298.83	H I	P28	−0.415	12	0.101	11	−38	0.112	11	1.104	*i*
8300.99	[Ni II]	2F	−0.416	–	–	–	−38	0.040	15	–	*g*
8306.11	H I	P27	−0.416	15	0.120	11	−36	0.129	11	1.075	*g*
8308.49	[Cr II]	1F	−0.416	–	–	–	−41	0.027	18	–	*g*
8314.26	H I	P26	−0.417	14	0.131	11	−37	0.154	9	1.173	
8323.42	H I	P25	−0.418	15	0.151	9	−36	0.171	9	1.138	
8333.78	H I	P24	−0.419	14	0.153	9	−38	0.173	9	1.131	
8345.55	H I	P23	−0.420	15	0.185	9	−36	0.189	9	1.026	*i*
8357.64	[Cr II]	1F	−0.422	–	–	–	−39	0.011	28	–	*g*
8359.00	H I	P22	−0.422	15	0.214	9	−37	0.241	9	1.128	*g*
8361.67	He I	1/6	−0.422	16	0.094	11	−35	0.091	11	0.968	*g*
8374.48	H I	P21	−0.423	15	0.233	9	−37	0.242	9	1.039	
8392.40	H I	P20	−0.425	14	0.248	9	−37	0.277	9	1.116	
8413.32	H I	P19	−0.427	14	0.277	9	−37	0.327	9	1.178	*g*, *i*
8437.96	H I	P18	−0.430	15	0.338	9	−37	0.353	9	1.045	
8446.25	O I	4	−0.431	30	0.566	9	−38	0.035	15	0.061	
8446.36	O I	4									
8446.76	O I	4	−0.635	27	0.279	9	–	–	–	–	
8446.76	O I	4	−0.431	27	0.282	9	–	–	–	–	
8467.25	H I	P17	−0.433	14	0.398	9	−37	0.403	9	1.012	*g*, *i*
8499.60	[Ni III]	1F	−0.436	–	–	–	−37	0.280	9	–	
8502.48	H I	P16	−0.436	15	0.453	9	−37	0.486	9	1.071	*i*
8665.02	H I	P13	−0.453	14	0.840	7	−38	0.835	7	0.994	
8728.90	[Fe III]	8F	−0.459	–	–	–	−37	0.105	11	–	*i*
8728.90	N I	21									
8733.43	He I	6/12	−0.459	13	0.033	15	−37	0.035	15	1.082	*g*
8736.04	He I	7/12	−0.460	15	0.010	28	−40	0.012	28	1.209	*g*
8750.47	H I	P12	−0.461	15	1.028	7	−37	1.032	7	1.004	
8838.20	[Fe III]	8F	−0.469	–	–	–	−41	0.064	11	–	*g*, *i*
8845.38	He I	6/11	−0.470	13	0.050	15	−36	0.054	15	1.068	
8848.05	He I	7/11	−0.470	6	0.023	18	−40	0.020	18	0.852	*g*, *i*
8862.79	H I	P11	−0.472	14	1.327	7	−37	1.311	7	0.987	
8891.91	[Fe II]	13F	−0.475	–	–	–	−41	0.397	9	–	
8914.77	He I	2/7	−0.477	13	0.022	18	−38	0.017	20	0.778	
8996.99	He I	6/10	−0.484	13	0.057	11	−38	0.059	11	1.022	
9014.91	H I	P10	−0.486	10	1.545	7	−37	1.764	7	1.141	*g*, *i*
9033.50	[Fe II]	13F	−0.488	–	–	–	−42	0.135	9	–	
9051.95	[Fe II]	13F	−0.489	–	–	–	−42	0.266	9	–	
9063.29	He I	4/8	−0.490	14	0.056	15	−36	0.053	15	0.944	
9068.60	[S III]	1F	−0.491	26	34.83	6	−28	37.41	6	1.074	
9123.60	[Cl II]	1F	−0.485	27	0.025	25	−35	0.078	15	3.117	
9210.28	He I	6/9	−0.494	14	0.078	11	−36	0.094	11	1.193	
9213.20	He I	7/9	−0.494	12	0.020	18	−39	0.033	15	1.710	
9226.62	[Fe II]	13F	−0.495	–	–	–	−42	0.233	9	–	
9229.01	H I	P9	−0.496	15	2.293	7	−37	2.330	7	1.015	
9267.56	[Fe II]	13F	−0.499	–	–	–	−42	0.168	9	–	*g*, *i*
9399.04	[Fe II]	13F	−0.512	–	–	–	−43	0.037	15	–	
9444.60	[Co III]	b^4P-b^4D	−0.517	–	–	–	−49	0.049	15	–	
9463.57	He I	1/5	−0.518	13	0.095	11	−37	0.127	9	1.341	
9526.16	He I	6/8	−0.524	14	0.094	11	−36	0.114	11	1.205	
9530.60	[S III]	1F	−0.525	26	80.05	6	−26	94.51	6	1.180	
9545.97	H I	P8	−0.526	15	3.301	7	−40	2.524	7	0.764	*i*
9701.20	[Fe III]	11F	−0.540	–	–	–	−27	0.214	9	–	
9705.30	[Ti III]	2F	−0.540	–	–	–	−34	0.019	18	–	
9903.46	C II	17.02	−0.557	14	0.048	40	−33	0.045	40	0.947	
9960.00	[Fe III]	8F	−0.562	–	–	–	−42	0.022	30	–	
10 027.7	He I	6/7	−0.567	14	0.152	9	−36	0.159	9	1.048	

Table 1 – *continued*

				Nebular component			Shock component				
λ_0 (Å)[a]	Ion[a]	Mult[a]	$f(\lambda)$[b]	V_{hel}[c]	$I(\lambda)$[d]	Error (per cent)[e]	V_{hel}[c]	$I(\lambda)$[d]	Error (per cent)[e]	I_{sh}/I_{neb}[f]	Notes
10 031.2	He I	7/7	−0.568	11	0.045	15	−38	0.054	11	1.185	
10 049.4	H I	P7	−0.569	13	5.425	7	−38	5.016	7	0.924	
10 320.5	[S II]	3F	−0.590	22	0.194	9	−37	1.016	7	5.234	
10 336.4	[S II]	3F	−0.591	22	0.216	9	−38	0.891	7	4.117	
10 370.5	[S II]	3F	−0.593	–	–	–	−38	0.396	9	–	

[a]Identification of each line: laboratory wavelength, ion and multiplet. Dubious identifications are marked with '?'.
[b]Value of the extinction curve adopted (Blagrave et al. 2007).
[c]Heliocentric velocity in units of km s^{-1}, the typical error is 1–2 km s^{-1}.
[d]Dereddened fluxes with respect to $I(H\beta) = 100$.
[e]Error of the dereddened flux ratios. Colons indicate errors larger than 40 per cent.
[f]Shock-to-nebular line flux ratio. See definition in equation (2).
[g]Line blended with another line and deblended via Gaussian fitting.
[h]Contaminated by 'ghost'.
[i]Contaminated by telluric emissions and not deblended.
[j]Deblended from telluric emissions.

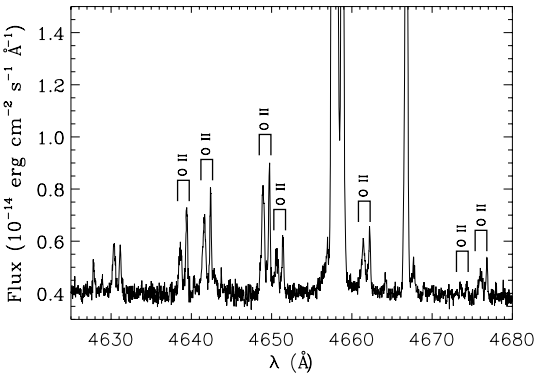

Figure 3. Section of the echelle spectrum of HH 202-S showing the shock (left-hand side) and nebular (right-hand side) components of each emission line of multiplet 1 of O II.

paper, we will provide and discuss further indications that HH 202-S contains an ionization front.

4.2 Physical conditions

We have computed physical conditions of the two kinematic components using several ratios of CELs following the same methodology as in Paper I and in Mesa-Delgado et al. (2008). The electron temperatures, T_e, and densities, n_e, are presented in Table 2.

We have determined n_e from [O II], [S II], [Cl III] and [Ar IV] line ratios using the NEBULAR package (Shaw & Dufour 1995). In the case of the n_e obtained from [Fe III] lines, we have used flux ratios of 31 and 12 lines for the shock and nebular components, respectively, following the procedure described by García-Rojas et al. (2006). For the nebular component, we have adopted the average value of n_e([O II]), n_e([S II]) and n_e([Cl III]) excluding n_e([Fe III]) and n_e([Ar IV]) due to their discrepant values and very large uncertainties. For the shock component, we have adopted the average of n_e([O II]), n_e([Cl III]) and n_e([Fe III]), while n_e([S II]) has not been included because the [S II] line ratio is out of the range of validity of the indicator. As we can see in Table 2, the density of the shock component ($\sim$17 000 cm^{-3}) is much higher than the density of the nebular one ($\sim$3000 cm^{-3}).

Table 2. Physical conditions.

Indicator		Nebular component	Shock component
n_e (cm^{-3})	[O II]	3490 ± 810	18 810 ± 8280
	[S II]	2350 ± 910	>14 200
	[Cl III]	2470 ± 1240	23 780 ± 13 960
	[Fe III]	11 800 ± 9000	17 100 ± 2500
	[Ar IV]	5800 :[a]	–
	Adopted	2890 ± 550	17 430 ± 2360
T_e (K)	[N II]	9610 ± 390	9240 ± 300
	[O II]	8790 ± 250	9250 ± 280
	[S II]	8010 ± 440	8250 ± 540
	[O III]	8180 ± 200	8770 ± 240
	[S III]	8890 ± 270	9280 ± 300
	[Ar III]	7920 ± 450	8260 ± 410
	He I	8050 ± 150	7950 ± 200

[a]Error larger than 60 per cent.

However, the bulk of the emission of the nebular component might come from behind HH 202, and the electron density that we have found for that component might not be the true one of the pre-shock gas. In fact, taking into account that the velocity of the gas flow is 89 km s^{-1} (O'Dell & Henney 2008) and the typical speed of sound in an ionized gas is about 10–20 km s^{-1}, we have adopted a Mach number, M, for HH 202 of about 5 and, thus, the shock compression ratio should be $M^2 \sim 25$. Using the density of the shock component (see Table 2), we obtain a pre-shock density $\sim$17 430/25 $\approx$ 700 cm^{-3}. This value is lower than the 2890 cm^{-3} determined for the nebular component. Therefore, it seems clear that the bulk of the nebular component does not refer to the gas in the immediate vicinity of HH 202 as we have mentioned in Section 2.

Electron temperatures have been derived from the classical CEL ratios of [N II], [O II], [S II], [O III], [S III] and [Ar III]. Under the two-zone ionization scheme, we have adopted T_e([N II]) as representative for the low-ionization zone and T_e([O III]) for the high-ionization zone. We have also derived T_e(He I) using the method of Peimbert, Peimbert & Luridiana (2002) and state-of-the-art atomic data (see Section 4.4).

We have compared these temperature determinations with those obtained from the integral field unit (IFU) data presented in Paper I.

We have determined the mean T_e values of the spaxels of the section of the field of view (FOV) of the PMAS data that encompasses the area covered by our UVES spectrum, finding $\langle T_e([O\,III])\rangle = 8760 \pm 260$ K and $\langle T_e([N\,III])\rangle = 9730 \pm 590$ K. These values are in agreement within the errors with those obtained in this paper (see Table 2). The average density from the IFU data, obtained from the [S II] line ratio, is 7300 ± 3000 cm^{-3}, a value between the n_e adopted for each kinematic component from the UVES data.

As we can see in Table 2, the T_e values are quite similar in both components with differences of the order of a few 100 K. The temperatures derived from [N II] lines are higher than those derived from [O III] lines, which is a typical result observed in previous works on the Orion Nebula (e.g. Rubin et al. 2003; Mesa-Delgado et al. 2008) as well as in Paper I. This is a likely result of the ionization stratification in the nebula. It is interesting to note that the difference between both temperatures is smaller in the case of the shock component, in this case all the emission comes from a – probably – much narrower slab of ionized gas.

The relatively low uncertainties in the physical conditions are due to the high signal-to-noise ratio of the emission lines used in the diagnostics. Blagrave et al. (2006) computed the physical conditions for HH 529 and they obtained similar results – higher densities in the shock component but similar temperatures in both components – though with comparatively larger errors.

4.3 Ionic abundances from CELs

Ionic abundances of N^+, O^+, O^{2+}, Ne^{2+}, S^+, S^{2+}, Cl^+, Cl^{2+}, Ar^{2+} and Ar^{3+} have been derived from CELs under the two-zone scheme and $t^2 = 0$, using the NEBULAR package. All abundances were calculated for the shock and nebular components, except for Ar^{3+}, which were not detected in the spectrum of the shock component. The atomic data for Cl^+ are not implemented in the NEBULAR routines, so we have used an old version of the five-level atom program of Shaw & Dufour (1995) – FIVEL – that is described by De Robertis, Dufour & Hunt (1987). This program uses the atomic data for this ion compiled by Mendoza (1983).

We have also measured [Ca II], [Cr II], [Fe II], [Fe III], [Fe IV], [Ni II] and [Ni III] lines. The abundances of these ions are also presented in Table 3. They were computed assuming the appropriate temperature under the two-zone scheme and the procedures indicated below. In addition and only in the shock component, we have detected a substantial number of lines of other quite rare heavy-element ions as [Cr III], [Co II], [Co III], [Ti III] and, possibly, [Cr IV], [Co IV], [Mn II] and [V II]. Unfortunately, we cannot derive abundances from these lines due to the lack of atomic data for these ions.

Two [Ca II] lines at 7291 and 7324 Å were detected in the shock component. In order to derive the Ca^+ abundance, we solved a five-level model atom using the single atomic data set available for this ion (Meléndez, Bautista & Badnell 2007). Note that this is the first determination of the Ca^+ abundance in the Orion Nebula and this poses a lower limit to the gas-phase Ca/H ratio in this object.

Two and four [Cr II] lines were measured in the nebular and shock components, respectively, although those at 8309 and 8368 Å are very faint. [Cr II] lines can be affected by continuum or starlight fluorescence as is also the case for the [Fe II] and [Ni II] lines. We have computed the Cr^+ abundances using a 180-level model atom that treat continuum fluorescence excitation as in Bautista, Peng & Pradhan (1996) and include the atomic data of Bautista et al. (2009). In order to consider the continuum fluorescence excitation, we have assumed that the incident radiation field derives entirely from the dominant ionization star θ^1 Ori C. As Bautista et al. (1996), we have calculated a dilution factor assuming a $T_{eff} = 39\,000$ K, $R_{star} = 9.0\,R_\odot$ (see Section 5.3) and a distance to the Orion Nebula of 414 pc (Menten et al. 2007). In Table 3, we include the Cr^+/H^+ ratio for the nebular and shock components. This is the first estimation of the Cr^+ abundance in the Orion Nebula.

Table 3. Ionic abundances and AD factors.

	Nebular component		Shock component	
	Ionic abundances from CELs			
	$t^2 = 0$	$t^2 > 0$	$t^2 = 0$	$t^2 > 0$
C^{2+}	7.87[b]	–	–	–
N^+	7.02 ± 0.04	7.07 ± 0.05	7.35 ± 0.03	7.52 ± 0.04
O^+	8.00 ± 0.06	8.05 ± 0.09	8.29 ± 0.06	8.48 ± 0.08
O^{2+}	8.35 ± 0.03	8.46 ± 0.04	8.08 ± 0.03	8.43 ± 0.05
Ne^{2+}	7.46 ± 0.11	7.58 ± 0.12	7.13 ± 0.10	7.51 ± 0.11
S^+	5.50 ± 0.07	5.54 ± 0.08	6.03 ± 0.04	6.22 ± 0.05
S^{2+}	6.90 ± 0.25	6.98 ± 0.25	6.89 ± 0.22	7.16 ± 0.21
Cl^+	3.99 ± 0.09	4.04 ± 0.10	4.52 ± 0.06	4.68 ± 0.06
Cl^{2+}	5.13 ± 0.04	5.23 ± 0.05	5.05 ± 0.05	5.38 ± 0.06
Ar^{2+}	6.30 ± 0.04	6.39 ± 0.04	6.26 ± 0.05	6.56 ± 0.04
Ar^{3+}	3.73 ± 0.11	3.85 ± 0.12	–	–
Ca^+	–	–	3.86 ± 0.07	4.03 ± 0.07
Cr^+	2.88 ± 0.11	2.92 ± 0.11	3.75 ± 0.07	3.91 ± 0.07
Fe^+	5.18 ± 0.26	5.23 ± 0.27	5.82 ± 0.03	6.01 ± 0.06
Fe^{2+}	5.66 ± 0.13	5.72 ± 0.13	6.77 ± 0.09	6.96 ± 0.10
Fe^{3+}	–	–	5.87 ± 0.16	6.16 ± 0.20
Ni^+	3.83 ± 0.10	3.88 ± 0.11	4.78 ± 0.09	4.96 ± 0.09
Ni^{2+}	4.42 ± 0.14	4.47 ± 0.15	5.60 ± 0.09	5.77 ± 0.09
	Ionic abundances from RLs			
He^+	10.94 ± 0.01		10.93 ± 0.01	
C^{2+}	8.32 ± 0.07		8.25 ± 0.08	
O^+	8.01 ± 0.12		8.25 ± 0.16	
O^{2+}	8.46 ± 0.03		8.44 ± 0.03	
	ADFs			
C^{2+}	0.45		-	
O^+	0.01 ± 0.17		-0.04 ± 0.14	
O^{2+}	0.11 ± 0.04		0.35 ± 0.05	

[a] In units of $12 + \log(X^{+n}/H^+)$.
[b] Average value from positions 8b and 11 of Walter et al. (1992).

Several [Fe II] lines have been detected in our spectra. As in the case of [Cr II] lines, most of them are affected by continuum fluorescence (see Rodríguez 1999; Verner et al. 2000). Following the same procedure as for Cr^+, we considered a 159 model atom in order to compute the Fe^+ abundances using the atomic data presented in Bautista & Pradhan (1998).

Many [Fe III] lines have been detected in the two kinematic components and their flux is not affected by fluorescence. For the calculations of the Fe^{2+}/H^+ ratio, we have implemented a 34-level model atom that uses collision strengths taken from Zhang (1996) and the transition probabilities of Quinet (1996) as well as the new transitions found by Johansson et al. (2000). The average value of the Fe^{2+} abundance has been obtained from 31 and 12 individual emission lines for the shock and nebular components, respectively.

One [Fe IV] line has been detected in the shock component at 6740 Å. The Fe^{3+}/H^+ ratio has been derived using a 33-level model atom where all collision strengths are those calculated by Zhang & Pradhan (1997) and the transition probabilities recommended by Froese Fischer & Rubin (2004).

Several [Ni II] lines have been measured in both kinematic components but they are strongly affected by continuum fluorescence (see Lucy 1995). As for the Cr^+ and Fe^+ ions, we have used a 76-level model that includes continuum fluorescence excitation and

the new collisional data of Bautista (2004) in order to compute the Ni^+ abundances.

We have measured several [Ni III] lines in the shock and nebular components. These lines are not expected to be affected by fluorescence. The Ni^{2+}/H^+ ratio has been derived using a 126-level model atom and the atomic data of Bautista (2001).

The final adopted values of the ionic abundances are listed in Columns (1) and (3) of Table 3 for the nebular and shock components, respectively. Columns (2) and (4) correspond to the ionic abundances of both components assuming the presence of temperature fluctuations (see Section 5.5). In this table, we have also included the C^{2+}/H^+ ratio obtained from UV CELs by Walter, Dufour & Hester (1992). We have taken the average of the values corresponding to their slit positions 8b and 11, the nearest positions to HH 202. The uncertainties shown in the table are the quadratic sum of the independent contributions of the error in the density, temperature and line fluxes.

The abundance determinations presented in Table 3 show the following behaviour: ionic abundances determined from CELs of once ionized species are always higher in the shock than in the nebular component; the twice-ionized species of elements lighter than Ne (included) show lower abundances in the shock than in the nebular component and the twice-ionized species of elements heavier than Ne show similar abundances in both components except for iron, chromium and nickel abundances that show substantially larger abundances in the shock component, something that can be explained if a significant dust destruction occurs in this component (see Section 5.6).

Finally, we have compared our abundance determinations from UVES data with those obtained in the HH 202-S region from the IFU data presented in Paper I. Integrating the spaxels of the section of the FOV indicated in Section 3, we obtain $12 + \log(O^{2+}/H^+) = 8.18 \pm 0.07$ from CELs, which is in good agreement with the numbers presented in Table 3 for both kinematic components. On the other hand, the average value of the O^+ abundance from CELs is 8.06 ± 0.14. However, considering the large density dependence of this ionic abundance, we have recalculated the O^+/H^+ ratio adopting the physical conditions measured in the shock component from UVES, finding a value of 8.26 ± 0.09, which is in better agreement with the UVES determinations for the shock component, the brightest one in the [O II] line emission.

4.4 Ionic abundances from RLs

We have measured several He I emission lines in the spectra of HH 202, both in the nebular and in the shock components. These lines arise mainly from recombination, but they can be affected by collisional excitation and self-absorption effects. We have used the effective recombination coefficients of Storey & Hummer (1995) for H I and those computed by Porter et al. (2005), with the interpolation formulae provided by Porter, Ferland & MacAdam (2007) for He I. The collisional contribution was estimated from Sawey & Berrington (1993) and Kingdon & Ferland (1995), and the optical depth in the triplet lines was derived from the computations by Benjamin, Skillman & Smits (2002). We have determined the He^+/H^+ ratio from a maximum likelihood method (MLM, Peimbert, Peimbert & Ruiz 2000; Peimbert, Peimbert & Luridiana 2002).

To self-consistently determine n_e(He I), T_e(He I), He^+/H^+ and the optical depth in the He I 3889 line, τ_{3889}, we have used the adopted density obtained from the CEL ratios for each component as n_e(He I) (see Table 2) and a set of 16 He I lines (at 3614, 3819, 3889, 3965, 4026, 4121, 4388, 4471, 4713, 4922, 5016, 5048, 5876, 6678, 7065 and 7281 Å). We have discarded the He I 5048 Å line in the nebular component because it is affected by charge transfer in the CCD. So, for the nebular component of HH 202, we have a total of 16 observational constraints (15 lines plus n_e), and for the shock component we have 17 observational constraints (16 lines plus n_e). Finally, we have obtained the best value for the three unknowns and t^2 by minimizing χ^2. The final χ^2 parameters we have obtained are 7.53 for the nebular component and 12.34 for the shock component, which indicate very good fits, taking into account the degrees of freedom. The final adopted value of the He^+/H^+ ratio for each component is included in Table 3.

We have detected C II lines of multiplets 2, 3, 4, 6 and 17.02. The brightest of these lines is C II 4267 Å, which belongs to multiplet 6 and can be used to derive a proper C^{2+}/H^+ ratio. The rest of the C II lines are affected by fluorescence, like multiplets 2, 3 and 4 (see Grandi 1976) or are very weak, as in the case of the line multiplet 17.02 that has an uncertainty of 40 per cent in the line flux.

We have derived the O^+/H^+ ratio from RLs for the shock and nebular components. The O I lines of multiplet 1 are very weak and they are partially blended with bright telluric emission. In order to obtain the best possible abundance determination, we have used different lines for each component: O I 7775 Å for the nebular component and O I 7772 Å for the shock one, these are precisely the lines least affected by line blending.

The high signal-to-noise ratio of the spectra allowed us to detect and measure seven lines of the multiplet 1 of O II as we can see in Fig. 3. These lines are affected by non-local thermal equilibrium (NLTE) effects (Ruiz et al. 2003), therefore to obtain a correct O^{2+} abundance it is necessary to observe the eight lines of the multiplet. However, these effects are rather small in the Orion Nebula – as well as in the observed components – due to its relatively large density. Then, assuming LTE, the O^{2+} abundance from RLs has been calculated considering the abundances obtained from the flux of each line of multiplet 1 and the abundance from the estimated total flux of the multiplet (see Esteban et al. 1998).

The abundance determinations in Table 3 show that the He^+/H^+, C^{2+}/H^+ and O^{2+}/H^+ ratios derived from RLs are always very similar in both shock and nebular components. In the case of O^+ abundances, the nominal values determined for both components seem to be somewhat different (about 0.24 dex), but they are marginally in agreement considering the large uncertainties of this ion abundance.

As in the previous section, we have compared our abundance determinations from RLs with those obtained for HH 202-S in Paper I. From the data of Paper I, we obtain $12 + \log(O^{2+}/H^+) = 8.39 \pm 0.13$ and $12 + \log(C^{2+}/H^+) = 8.29 \pm 0.11$, values which are in good agreement with those obtained in this paper.

4.5 Abundance discrepancy factors

We have calculated ionic abundances from two kinds of lines – RLs and CELs – for three ions: C^{2+}, O^+ and O^{2+}. We present their values for the two components in Table 3. We have computed the ADF for these ions using the following definition:

$$\mathrm{ADF}(X^{+i}) = \log\left(\frac{X^{+i}}{H^+}\right)_{RL} - \log\left(\frac{X^{+i}}{H^+}\right)_{CEL}. \quad (3)$$

In the case of the ADF(C^{2+}), it can only be estimated for the nebular component and from the comparison of our determination from RLs and those from CELs for nearby zones taken from the literature. The value of the ADF(C^{2+}) amounts to 0.45 dex.

On the one hand, the ADF(O^+) can also be estimated in our spectrum and shows values very close to zero. However, these ADF

values are rather uncertain. On the other hand, as we can see in Table 3, the O^{2+} abundance from RLs is the same for both components while that from CELs is lower in the shock component, probably because the recombination rate increases in the shock one. This fact produces an ADF(O^{2+}) about 0.2 dex higher in the shock component than in the nebular one. This striking result will be discussed in Section 5.5.

The values of the ADFs of C^{2+} and O^{2+} for the nebular component are in good agreement with those obtained by Esteban et al. (2004) for a zone closer to the Trapezium cluster than HH 202. In the case of the ADF(O^+), both determinations disagree, Esteban et al. (2004) report a much larger value (0.39 dex).

4.6 Total abundances

In order to derive the total gaseous abundances of the different elements present in our spectrum, we have to correct for the unseen ionization stages by using a set of ionization correction factors (ICFs). The adopted ICF values are presented in Table 4 and the total abundances in Table 5. As in the case of the ionic abundances from CELs, these tables include values under the assumption of $t^2 = 0$ (Columns 1 and 3) and under the presence of temperature fluctuations (see Section 5.5; Columns 2 and 4).

The total helium abundance has been corrected for the presence of neutral helium using the expression proposed by Peimbert, Torres-Peimbert & Ruiz (1992) based on the similarity of the ionization potentials (IPs) of He^0 (24.6 eV) and S^+ (23.3 eV):

$$\frac{He}{H} = \left(1 + \frac{S^+}{S - S^+}\right) \times \frac{He^+}{H^+} = ICF(He^0) \times \frac{He^+}{H^+}. \quad (4)$$

For C, we have adopted the ICF(C^+) derived from photoionization models of Garnett et al. (1999) for the shock and nebular components. In order to derive the total abundance of nitrogen, we have used the usual ICF:

$$\frac{N}{H} = \frac{O^+ + O^{2+}}{O^+} \times \frac{N^+}{H^+} = ICF(N^{2+}) \times \frac{N^+}{H^+}. \quad (5)$$

Table 4. Adopted ICF values.

		Nebular component		Shock component	
Elements	Unseen ion	$t^2 = 0$	$t^2 > 0$	$t^2 = 0$	$t^2 > 0$
He	He^0	1.04 ± 0.02	1.03 ± 0.02	1.12 ± 0.06	1.08 ± 0.04
C[a]	C^+	1.31 ± 0.46		1.50 ± 0.47	
N	N^{2+}	3.21 ± 0.54	3.82 ± 0.83	1.62 ± 0.27	2.29 ± 0.46
Ne	Ne^+	1.45 ± 0.15	1.35 ± 0.19	2.61 ± 0.31	1.78 ± 0.26
S	S^{3+}	1.01 ± 0.01	1.01 ± 0.01	1.09 ± 0.03	1.03 ± 0.01
Ar[b]	Ar^+	1.33	–	–	–
Ar[c]	Ar^+	1.20 ± 0.36	1.16 ± 0.36	2.00 ± 0.51	1.71 ± 0.46
Fe[d]	Fe^{3+}	2.71 ± 0.46	3.16 ± 0.69	1.52 ± 0.25	2.02 ± 0.41
Ni	Ni^{3+}	3.21 ± 0.54	3.82 ± 0.83	1.62 ± 0.27	2.29 ± 0.46

[a]From photoionization models by Garnett et al. (1999).
[b]Mean of Orion Nebula models.
[c]From correlations obtained by Martín-Hernández et al. (2002).
[d]From photoionization models by Rodríguez & Rubin (2005).

Table 5. Total abundances.[a]

	Nebular component		Shock component	
	$t^2 = 0$	$t^2 > 0$	$t^2 = 0$	$t^2 > 0$
He	10.95 ± 0.01	10.95 ± 0.02	10.98 ± 0.03	10.98 ± 0.02
C[b]	8.07	–	–	–
C[c]	8.43 ± 0.17		8.43 ± 0.16	
N	7.53 ± 0.08	7.62 ± 0.11	7.56 ± 0.08	7.81 ± 0.10
O	8.51 ± 0.03	8.60 ± 0.04	8.50 ± 0.04	8.76 ± 0.05
O[c]	8.59 ± 0.05		8.65 ± 0.05	
Ne	7.62 ± 0.12	7.72 ± 0.13	7.54 ± 0.11	7.83 ± 0.12
S	6.92 ± 0.24	7.00 ± 0.24	6.98 ± 0.19	7.23 ± 0.19
Cl	5.16 ± 0.04	5.26 ± 0.05	5.16 ± 0.04	5.46 ± 0.05
Ar[d]	6.42 ± 0.04	6.52 ± 0.04	–	–
Ar[e]	6.38 ± 0.19	6.46 ± 0.14	6.56 ± 0.21	6.79 ± 0.12
Fe[f]	–	–	6.86 ± 0.07	7.06 ± 0.08
Fe[g]	6.10 ± 0.15	6.19 ± 0.16	6.95 ± 0.12	7.19 ± 0.13
Ni	5.03 ± 0.14	5.12 ± 0.15	5.87 ± 0.11	6.11 ± 0.12

[a]In units of $12 + \log(X^{+n}/H^+)$.
[b]Average value from positions 8b and 11 of Walter et al. (1992).
[c]Value derived from RLs.
[d]Adopting the ICF from the mean of Orion Nebula models.
[e]Adopting the ICF from *ISO* observations (Martín-Hernández et al. 2002).
[f]From $Fe^+ + Fe^{2+} + Fe^{3+}$.
[g]Assuming the ICF of equation (6).

This expression gives very different values of the ICF(N^{2+}) for both components due to their rather different ionization degree.

The total abundance of oxygen is calculated as the sum of O^+ and O^{2+} abundances. The absence of He II lines in the spectra, and the similarity between the IPs of He^+ and O^{2+}, implies the absence of O^{3+}. In Table 5, we present the O abundances from RLs and CELs.

The only measurable CELs of Ne in the optical range are those of Ne^{2+} but the fraction of Ne^+ can be important in the nebula. We have adopted the usual expression (Peimbert & Costero 1969) to obtain the total Ne abundance:

$$\frac{\mathrm{Ne}}{\mathrm{H}} = \frac{\mathrm{O}^+ + \mathrm{O}^{2+}}{\mathrm{O}^{2+}} \times \frac{\mathrm{Ne}^{2+}}{\mathrm{H}^+} = \mathrm{ICF}(\mathrm{Ne}^+) \times \frac{\mathrm{Ne}^{2+}}{\mathrm{H}^+}. \quad (6)$$

We have measured CELs of two ionization stages of S: S^+ and S^{2+}. Then, we have used an ICF to take into account the presence of S^{3+} (Stasińska 1978) which is based on photoionization models of H II regions,

$$\frac{\mathrm{S}}{\mathrm{H}} = \left[1 - \left(\frac{\mathrm{O}^+}{\mathrm{O}^+ + \mathrm{O}^{2+}}\right)^3\right]^{-1/3} \frac{\mathrm{S}^+ + \mathrm{S}^{2+}}{\mathrm{H}^+} = \\ = \mathrm{ICF}(\mathrm{S}^{3+}) \times \frac{\mathrm{S}^+ + \mathrm{S}^{2+}}{\mathrm{H}^+}. \quad (7)$$

Following Esteban et al. (1998), we expect that the amount of Cl^{3+} is negligible in the Orion Nebula. Therefore, the total abundance of chlorine is simply the sum of Cl^+ and Cl^{2+} abundances.

For argon, we have determinations of Ar^{2+} and Ar^{3+} but some contribution of Ar^+ is expected. In Table 4, we present the values obtained from two ICF schemes: one obtained from correlations between N^{2+}/N^+ and Ar^{2+}/Ar^+ from *Infrared Space Observatory* (*ISO*) observations of compact H II regions by Martín-Hernández et al. (2002) and another one – following Osterbrock, Tran & Veilleux (1992) – derived as the mean of Orion Nebula models by Rubin et al. (1991) and Baldwin et al. (1991).

We have measured lines of three ionization stages of iron in the shock component – Fe^+, Fe^{2+} and Fe^{3+} – and two stages of ionization in the nebular component – Fe^+ and Fe^{2+}. For the shock component, we can derive the total Fe abundance from the sum of the three ionization stages. For the nebular component – and also for the shock one in order to compare – we have used an ICF scheme based on photoionization models of Rodríguez & Rubin (2005) to obtain the total Fe/H ratio using only the Fe^{2+} abundances, which is given by

$$\frac{\mathrm{Fe}}{\mathrm{H}} = 0.9 \times \left(\frac{\mathrm{O}^+}{\mathrm{O}^{2+}}\right)^{0.08} \times \frac{\mathrm{Fe}^{2+}}{\mathrm{O}^+} \times \frac{\mathrm{O}}{\mathrm{H}}. \quad (8)$$

Finally, there is no ICF available in the literature to correct for the presence of Ni^{3+} in order to calculate the total Ni abundance. Nevertheless, we have applied a first-order ICF scheme based on the similarity between the IPs of Ni^{3+} (35.17 eV) and O^{2+} (35.12 eV):

$$\frac{\mathrm{Ni}^{3+}}{\mathrm{Ni}} = \frac{\mathrm{O}^{2+}}{\mathrm{O}}. \quad (9)$$

Therefore,

$$\frac{\mathrm{Ni}}{\mathrm{H}} = \frac{\mathrm{O}}{\mathrm{O}^+} \times \left(\frac{\mathrm{Ni}^+}{\mathrm{H}^+} + \frac{\mathrm{Ni}^{2+}}{\mathrm{H}^+}\right). \quad (10)$$

In general, the total abundances shown in Columns (1) and (3) of Table 5 are quite similar for the shock and nebular components within the errors, except for the nickel and iron abundances, which are much larger in the shock component – see Section 5.6 for a possible explanation. The set of abundances for the nebular component are in very good agreement with previous results of Esteban et al. (2004). We have also compared our Ni abundance values with the previous determination of Osterbrock et al. (1992) finding that our Ni/H ratio for the nebular component is an order of magnitude lower. This difference is due to the large uncertainties in the atomic data used by those authors (see Bautista 2001).

5 DISCUSSION

5.1 Differences between the $c(\mathrm{H}\beta)$ coefficient determined with different lines

A puzzling feature of our UVES data is that the $c(\mathrm{H}\beta)$ values determined with different lines ratios appear to be inconsistent with each other, even with observational errors taken into account. Possible explanations are either a bias in the extinction curve or an extra mechanism, in addition to extinction, altering the individual line intensities from case B predictions.

Fig. 4 shows the $c(\mathrm{H}\beta)$ values measured for individual line ratios in the Balmer and Paschen series. The bizarre pattern followed by the curve, and particularly the steep slope it reaches in the proximity of the Balmer and Paschen limits, strongly suggests that the solution cannot be a bias in the extinction law.

We can test the second hypothesis by considering how the line intensity ratios relative to case B ratios depend on the principal quantum number n of the level where each line originates. Such dependence, plotted in Fig. 5 for the two kinematic components, shows a definite trend with n for both series. This strongly supports the second of our hypotheses, namely that an extra mechanism is acting to deviate level populations away from case B predictions. Indeed, detailed photoionization modelling indicates that this behaviour is the result of two independent but concomitant mechanisms: ℓ-changing collisions with $|\Delta\ell| > 1$ and pumping of Balmer and Paschen lines by absorption of stellar continuum photons at the Lyman wavelengths. Both mechanisms are neglected in case B calculations (Storey & Hummer 1995) but included in our models, which take advantage of a new model hydrogen atom with fully resolved levels (CLOUDY, version C08.00; Porter, Ferland, van Hoof, & Williams, in preparation; see also appendix A in Luridiana et al. 2009); both alter the n, ℓ populations, resulting in enhanced intensities of the high-n lines.

As for the first mechanism, at low n it has a negligible effect if compared to other depopulation mechanisms, such as

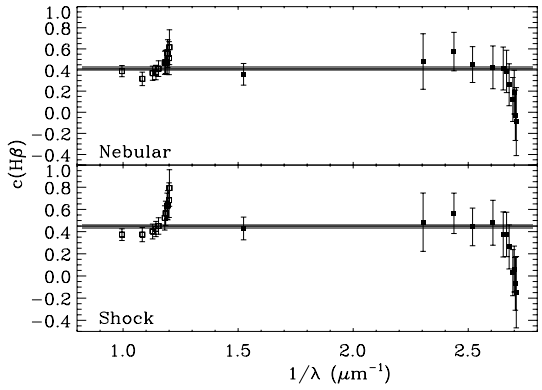

Figure 4. $c(\mathrm{H}\beta)$ values obtained from different line ratios versus the inverse of the wavelength in μm for the nebular (up) and shock component (down). The filled and non-filled squares correspond to the $c(\mathrm{H}\beta)$ values derived from Balmer and Paschen lines, respectively. The horizontal line is the weighted average value adopted and the grey band its error.

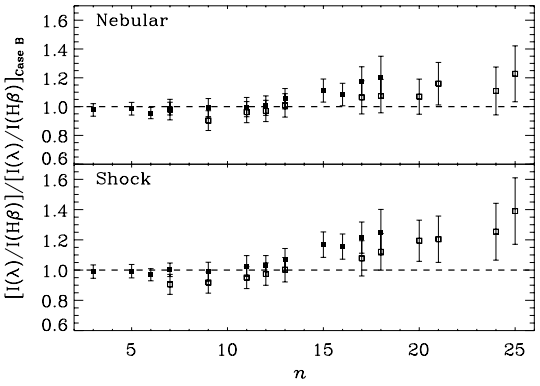

Figure 5. Dereddened fluxes of Balmer (filled squares) and Paschen (non-filled squares) lines to their theoretical flux under the case B prediction ratio versus the principal quantum number n for the nebular (up) and shock components (down).

energy-changing collisions and horizontal collisions with $|\Delta\ell| = 1$; at high n, it becomes increasingly important. Case B calculations neglect this mechanism by construction, so a discrepancy is doomed to appear whenever high-n lines are compared to case B results.

The effectiveness of the second mechanism strongly depends on the availability of the exciting photons, i.e. on the stellar flux at the Lyman wavelengths; the results of Luridiana et al. (2009) and further preliminary calculations (Luridiana et al., in preparation) suggest that its impact on line intensities might increase with n.

A full account of both processes in H II regions can be found in Luridiana et al. (2009) and Luridiana et al. (in preparation).

5.2 Comparison of line ratios in the shock and nebular components and the ionization structure

To maximize the shock-to-nebula ratio, the echelle spectra were extracted over the area where the shock component is brighter and the velocity separation with respect to the nebular background gas is maximum (see Fig. 2).

In Fig. 6, we present the weighted average shock-to-nebular ratio for different ionic species, $I(\lambda)_{sh}/I(\lambda)_{neb}$ – which was defined in equation (1) – with respect to the IP needed to create the associated originating ion. In general, as we can see in this figure, the line ratios of the shock component relative to those of the ambient gas

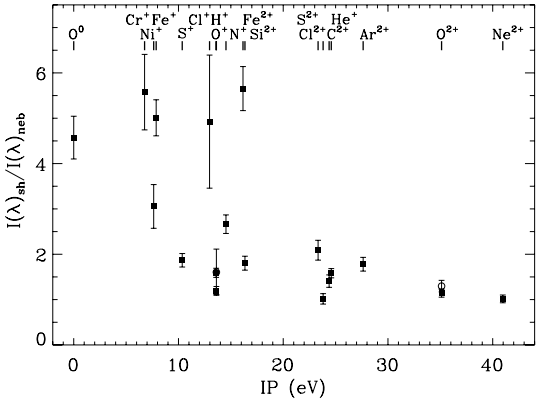

Figure 6. Weighted average of shock-to-nebular line ratios versus the IP needed to create the associated originating ion. Non-filled circles correspond to ratios measured from RLs (only for O^+ and O^{++}). Smaller error bars are of about 3 per cent.

are between 1 and 2 for most ionic species with IP above 10 eV and close to one for the most ionized species as O^{2+} and Ne^{2+}. Since the illumination of the shock should be approximately the same as that of the nebula at this particular zone of the slit, shock-to-nebular ratios of the order of one imply that the shock should be ionization-bounded. This is exactly the opposite situation that Blagrave et al. (2006) find in HH 529, where the shock-to-nebular ratios are clearly lower than 1 indicating that the shock associated to HH 529 is matter-bounded.

As we have commented above and can be seen in Fig. 6, the shock-to-nebular ratio varies from 1 to 2 for species with an IP higher than 10 eV except in two cases: (i) Fe^{2+}, whose lines show a substantial enhancement in the shock component, probably due to dust destruction (see Section 5.6) and (ii) Cl^+, but this can be accidental because this ionic abundance is derived from a single rather faint line with a very large uncertainty. Ionic species with an IP lower than 10 eV show a shock-to-nebular ratio always higher than 2 in Fig. 6. In particular, Fe^+, Ni^+ and Cr^+ show ratios larger than 2 and these ions may be also affected by an increase of the gas-phase abundance due to dust destruction.

Neutral species like O^0 or N^0 are associated with the presence of an ionization front. In the case of O^0, the shock-to-nebular ratio has been calculated from the [O I] 6300 and 6363 Å lines that are contaminated by telluric emissions but only in the shock component. We extracted the telluric emissions from the zone free of shock emission along the slit and subtracted this feature to the shock component. The shock-to-nebular ratio of [O I] lines is the largest one for those ions which are not heavily affected by possible dust destruction. This is a further indication of the presence of an ionization front in HH 202-S. In the case of [N I] lines, those belonging to the nebular component are also contaminated by telluric emission but, in this case, it was impossible to deblend properly these lines.

In Fig. 2, we can see the spatio-kinematic profiles of lines of different ionization stages of oxygen: O^0, O^+ and O^{2+}, including RLs and CELs. In the shock component, we can clearly distinguish a stratification in the location of the ions: the bulk of the O^{2+} emission is located at the south of the extracted area, O^0 at the north and O^+ is located approximately at the centre of the extracted area. Another interesting feature that can be seen in Fig. 2 is that the emissions from RLs and CELs of the same ion seem to show the same spatio-kinematic profiles. These profiles provide further indication that HH 202-S is an ionization-bounded shock.

The peak emission of the spatio-kinematic profiles of ions with IP lower or similar to the one of O^+: Cr^+, Ni^+, S^+, Fe^+ or H^+ is located to the north of HH 202-S, as in the case of O^+. Ions as He^+, C^{2+} or Fe^{2+} show their peak emission about the centre of the aperture, while the ions with the highest IP, as Ne^{2+} or Ar^{3+}, show spatio-kinematic profiles similar to that of O^{2+}.

5.3 Width of the ionized slab and the physical separation between θ^1Ori C and HH 202-S

An interesting result of this paper is the claim that HH 202-S contains an ionization front as we have shown in Sections 4.1 and 5.2. Due to this fact, we can estimate the width of the ionized slab of HH 202-S and its physical separation with respect to the main ionization source of the Trapezium cluster, θ^1Ori C.

On the one hand, from the maximum emission of the shock component in the spatio-kinematic profiles of O^{2+} and O^0 shown in Fig. 2, we can measure an angular distance on the plane of the sky of about 3.9 ± 0.5 arcsec. Using the distance to the Orion Nebula obtained by Menten et al. (2007), $d = 414 \pm 7$ pc, and

the inclination angle of HH 202-S with respect to the plane of the sky calculated by O'Dell & Henney (2008), $\theta = 48^{\circ}$, we estimate $(11.7 \pm 1.5) \times 10^{-3}$ pc for the width of the ionized slab.

On the other hand, to trap the ionization front in HH 202-S, the incident Lyman continuum flux must be balanced by the recombinations in the ionized slab, i.e.

$$F_{\rm Ly} = \frac{Q(H^0)}{4\pi D^2} = n_{\rm sh}^2 \alpha_B(H^0, T) L, \quad (11)$$

where D is the physical separation between HH 202-S and θ^1Ori C, $Q(H^0)$ is the ionizing photon rate, $n_{\rm sh}$ the density in the shock component, $\alpha_B(H^0, T)$ is the case B recombination coefficient for H and L is the width of the slab. In order to estimate $Q(H^0)$, we have used a spectral energy distribution of FASTWIND code with the stellar parameters for θ^1Ori C obtained by Simón-Díaz et al. (2006) – $T_{\rm eff} = 39\,000 \pm 1000$ K and $\log g = 4.1 \pm 0.1$ dex – and the distance to the Orion Nebula calculated by Menten et al. (2007). Then, the output parameters have been: the stellar radius $R = (9.0 \pm 1.3)$ $R_{\odot}$, the stellar luminosity $\log L = 38.80 \pm 0.14$ dex and the ionizing photon rate $Q(H^0) = (6.30 \pm 2.00) \times 10^{48}$ s^{-1}. Taking a value for the recombination coefficient, $\alpha_B = 2.59 \times 10^{-13}$ cm^{-3} s^{-1} at 10^4 K, we have finally calculated a physical separation of $D = 0.14 \pm 0.05$ pc. This result suggests that HH 202 is quite embedded within the body of the Orion Nebula and, therefore, discards the origin of the ionized front as result of the interaction of the gas flow with the veil (see Section 4.1), which is between 1 and 3 pc in front of the Trapezium cluster (see Abel et al. 2004).

5.4 Radial velocity analysis

In Fig. 7, we show the average heliocentric velocity of the lines that belong to a given ionic species as a function of the IP needed to create the associated originating ion. We have used two separate graphs to distinguish between the behaviour of the nebular and the shock components. The nebular component shows the typical velocity gradient that has been observed in other positions of the Orion Nebula and other H II regions (e.g. Bautista & Pradhan 1998; Esteban & Peimbert 1999), with a velocity difference of the order of -15 km s^{-1} between the neutral and the most ionized species. This gradient is likely produced by the presence of flows of ionized gas originating from the ionization front inside the nebula. In contrast, the ions in the shock component show a rather similar radial velocity independently of their IP. This indicates that the bulk of the ionized gas at the HH 202-S is moving at approximately the same velocity with respect to the rest of the nebula. The H II lines (Balmer and Paschen series) of the shock component are shifted by -50.7 ± 1.0 km s^{-1} relative to the H II lines of the nebular component and -64.8 ± 1.0 km s^{-1} relative to the velocity of the photon-dominated region (PDR,+28 km s^{-1}; Goudis 1982). The zone covered by our UVES slit (see Fig. 1) coincides with position 117−256 of Doi et al. (2004). These authors detect two radial velocity components belonging to the shock gas in this zone, a fast component (-57 km s^{-1}) and a slower brighter one (-31 km s^{-1}). Our value of the radial velocity for the shock component of HH 202 (-36.8 ± 1.0 km s^{-1}) is somewhat more negative than the slower velocity component of Doi et al. (2004), probably our shock component corresponds to the unresolved blend of the two velocity systems detected by those authors.

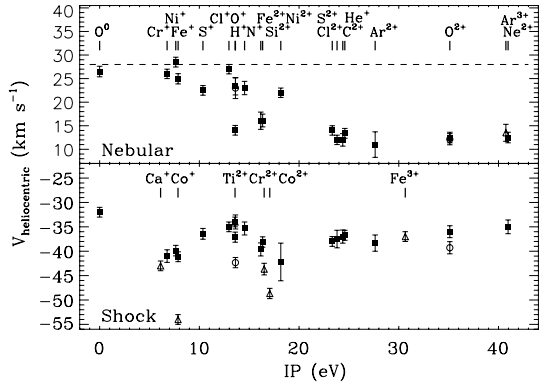

Figure 7. Heliocentric velocities of the nebular (up) and shock (down) components emission lines versus the IP needed to create the associated originating ion. The velocity of the PDR (dashed horizontal line) is also shown. Non-filled triangles correspond to ions observed in only one kinematic component. Non-filled circles correspond to heliocentric velocities measured from RLs (only for O^+ and O^{++}).

5.5 The abundance discrepancy and temperature fluctuations

Assuming the validity of the temperature fluctuations paradigm and that this phenomenon produces the AD, we can estimate the values of the t^2 parameter from the ADFs obtained for each component and ion (see Table 3). In Table 6, we include the t^2 values that produce the agreement between the abundance determinations obtained from CELs and RLs of O^{2+} and C^{2+}. These calculations have been made following the formalism outlined by Peimbert & Costero (1969). Adopting the t^2 value obtained for O^{2+} zone, $t^2(O^{2+})$, we have calculated the ionic abundances, the ICFs and the total abundances under the presence of temperature fluctuations and they are presented in Tables 3–5, respectively.

As we can see in Table 5, the high $t^2(O^{2+})$ value used to derive the abundances for the shock component implies that the total abundances obtained from CELs considering $t^2 > 0$ are higher in the shock component than in the nebular one for all the elements. On the other hand, the abundances of C and O obtained from RLs are very similar in both components. Moreover, the O/H ratio computed from CELs for $t^2 > 0$ is higher than that obtained from RLs. However, for the nebular component, we find that the total abundance of oxygen determined from CELs considering $t^2 > 0$ agrees with the oxygen abundance from RLs.

These results can suggest that, perhaps, the t^2 value we have found for the shock component is too high and, therefore, that the

Table 6. Estimates of the t^2 parameter.

	HH 202		HH 529[a]		
Ion	Nebular component	Shock component	Nebular component	Shock component	Esteban et al. (2004)
O^{2+}	0.016 ± 0.006	0.050 ± 0.007	0.009 ± 0.004	0.010 ± 0.010	0.022 ± 0.002
C^{2+}	0.040	–	–	–	0.039 ± 0.011
He^+	0.014 ± 0.013	0.049 ± 0.011	–	–	–

[a]Blagrave et al. (2006).

t^2 paradigm is not applicable in this case. However, we have to consider that we have used a t^2 value representative of the high-ionization zone for all the ions. The increase of the O^+/O^{2+} ratio in the shock component with respect to the nebular one, due to an enhanced recombination rate, makes the O^+ zone more extended in this component and a lower $t^2(O^+)$ would lead to a better agreement between the O abundances of both components. We have also computed the t^2 parameter for the He^+ zone using a MLM (see Section 4.4). The determination of the $t^2(He^+)$ weighs the O^+ and the O^{2+} zones depending on their extension. It is remarkable that the t^2 values obtained from different methods, such as the He^+ lines and the ADF(O^{2+}), which assume the presence of temperature fluctuations in the observed volume, produce almost identical values in both components, though $t^2(He^+)$ has large uncertainties. These ones can reconcile the total abundances of both components for $t^2 > 0$ considering that the MLM depends strongly on the He I 3889 Å line flux and that the shock components of this line and H8 are severely blended.

In Table 6, we have also included the values of t^2 obtained by Blagrave et al. (2006) from the ADF(O^{2+}) that they estimate for the nebular and shock components of HH 529 and those obtained by Esteban et al. (2004) from the ADF of O^{2+} and C^{2+}. The data of Esteban et al. (2004) correspond to a zone free of high-velocity flows and can be considered as representative of the nebular component but closer to the Trapezium. The values of the t^2 obtained for the nebular component of HH 202-S are quite consistent with those obtained by Esteban et al. (2004). The $t^2(O^{2+})$ of the nebular component of HH 529 obtained by Blagrave et al. (2006) is lower than the two other determinations, but still consistent with our values within the uncertainties. As has been commented above, the t^2 values found in the shock component of HH 202 are much higher than those of the nebular component and the value determined by Blagrave et al. (2006) for the shock component of HH 529.

The effect of temperature fluctuations in the spectra of ionized nebulae and their existence has been a controversial problem from the first work of Peimbert (1967). Peimbert (1995), Esteban (2002), Peimbert & Peimbert (2006) have reviewed the possible mechanisms that could produce such temperature fluctuations. Among the possible sources of temperature fluctuations, we can list the deposition of mechanics energy by shocks and the gas compression due to turbulence. Peimbert, Sarmiento & Fierro (1991) have studied the effect of shock waves in H II regions using shock models by Hartigan et al. (1987). They found that high t^2 values can be explained by the presence of shocks with velocities larger than 100 km s^{-1}. In the case of the flow of 89 km s^{-1} that produces HH 202, this effect should produce very small t^2 values. Therefore, another process or other formalisms of the problem should be taken into account in this case. Further discussion of this problem is beyond the scope of this article.

5.6 Dust destruction

As indicated in Section 5.2, the emission lines of refractory elements as Fe, Ni or Cr are much brighter in the gas flow than in the ambient gas. Moreover, the shock component shows relatively bright [Ca II] lines which are not detected in the spectrum of the ambient gas. On the other hand, in Section 4.1 we have stated that HH 202-S does not contain a substantial contribution of shock excitation and, therefore, we need other mechanisms to explain those abnormally high line fluxes. It is well known that Fe, Ni, Cr and Ca are expected to be largely depleted in neutral and molecular interstellar clouds as well as in H II regions. However, theoretical studies have shown that fast shocks – as those typical in HH objects and supernova remnants – should efficiently destroy grains by thermal and non-thermal sputtering in the gas behind the shock front and by grain–grain collisions (McKee, Chernoff & Hollenbach 1984; Jones et al. 1994; Mouri & Taniguchi 2000). Several works have shown that some non-photoionized HH flows show a decrease in the amount of Fe depletion as determined from the analysis of [Fe II] lines (Beck-Winchatz, Bohm & Noriega-Crespo 1996; Böhm & Matt 2001; Nisini et al. 2005). On the other hand, HH 399 is the first precedent of a fully ionized HH object where an overabundance in Fe was detected and this one was related with dust destruction (Rodríguez 2002).

In Table 7, we compare the values of the C, O, Fe, Ni and Cr^+ abundances and the Fe/Ni ratios of the Sun (Grevesse, Asplund & Sauval 2007) and the nebular and shock components for $t^2 = 0$ and $t^2 > 0$. In the case of Fe and Ni, we can see that the difference between the abundances of the shock and nebular components are of the order of 0.85 dex for $t^2 = 0$ and 1.00 dex for $t^2 > 0$. This result indicates that the gas-phase abundance of Fe and Ni increases by a factor between 7 and 10 after the passage of the shock wave. The fact that the Fe/Ni ratio is the same in both

Table 7. Comparison of abundances and depletion factors.

		Nebular component		Shock component	
	Sun[a]	$t^2 = 0$	$t^2 > 0$	$t^2 = 0$	$t^2 > 0$
C	8.39 ± 0.05	8.43 ± 0.17		8.43 ± 0.16	
O	8.66 ± 0.05	8.59 ± 0.05		8.65 ± 0.05	
Fe	7.45 ± 0.05	6.10 ± 0.15	6.19 ± 0.16	6.95 ± 0.12	7.19 ± 0.13
Ni	6.23 ± 0.04	5.03 ± 0.14	5.12 ± 0.15	5.87 ± 0.11	6.11 ± 0.12
Fe/Ni	1.22 ± 0.06	1.07 ± 0.23	1.07 ± 0.25	1.08 ± 0.17	1.08 ± 0.19
Cr^+	-	2.88 ± 0.11	2.92 ± 0.11	3.75 ± 0.07	3.91 ± 0.07
	Shock−Nebular		Nebular−Sun		Shock−Sun	
	$t^2 = 0$	$t^2 > 0$	$t^2 = 0$	$t^2 > 0$	$t^2 = 0$	$t^2 > 0$
C	0.00 ± 0.27		0.04 ± 0.19		0.04 ± 0.18	
O	0.06 ± 0.07		-0.07 ± 0.07		-0.01 ± 0.07	
Fe	0.85 ± 0.13	1.00 ± 0.14	-1.35 ± 0.05	-1.26 ± 0.05	-0.50 ± 0.06	-0.26 ± 0.09
Ni	0.84 ± 0.12	0.99 ± 0.13	-1.20 ± 0.04	-1.11 ± 0.04	-0.36 ± 0.06	-0.12 ± 0.10
Fe/Ni	–	–	–	–	–	–
Cr^+	0.87 ± 0.07	0.99 ± 0.07	–	–	–	–

[a] Grevesse et al. (2007).

components – because the increase of the gas-phase abundance of both elements is the same – and consistent with the solar Fe/Ni ratio within the errors suggests that the abundance pattern we see in HH 202-S is the likely product of dust destruction. In fact, observations of Galactic interstellar clouds indicate that Fe, Ni – as well as Cr – have the same dust-phase fraction (Savage & Sembach 1996b; Jones 2000). It is also remarkable that, although it could be modulated by ionization effects, the behaviour of the Cr^+ abundance is also consistent with the dust-destruction scenario. The increase of the Cr^+/H^+ ratio between the nebular and shock components is identical to that of Fe and Ni.

Considering the solar Fe/H ratio as the reference ($12 + \log(Fe/H) = 7.45 \pm 0.05$; Grevesse et al. 2007) – which is almost identical to the Fe/H ratio determined for the B-type stars of the Orion association ($12 + \log(Fe/H) = 7.44 \pm 0.04$; Przybilla, Nieva & Butler 2008) – we estimate that the Fe dust-phase abundance decreases by about 30 per cent for $t^2 = 0$ and about 53 per cent for $t^2 > 0$ after the passage of the shock wave in HH 202-S. This result is in good agreement with the predictions of the models of Jones et al. (1994) and Mouri & Taniguchi (2000). In particular, for the velocity determined for HH 202 (89 km s^{-1}; O'Dell & Henney 2008), Jones et al. (1994) obtain a level of destruction of iron dust particles of the order of 40 per cent. On the other hand, the Fe gas-phase abundance we measure in HH 202-S follows closely the empirical correlation obtained by Böhm & Matt (2001) from [Fe II] and [Ca II] emission line fluxes of several non-photoionized HH flows. Further evidence that the dust is not completely destroyed in HH 202 is the detection of 11.7 μm emission coincident with the bright ionized gas around HH 202-S (Smith et al. 2005). As we can see in Table 7, the depletion factors of Fe and Ni in the nebular component are similar to those found in warm neutral interstellar environments and those at HH 202-S of the order of the depletions observed in the Galactic halo (see Welty et al. 1999 and references therein).

In the cases of C and O, the effect of dust destruction in their gas-phase abundance is more difficult to estimate. First, these elements are far less depleted in dust grains than Fe or Ni in neutral interstellar clouds and in H II regions. Secondly, there is still a controversy about the correct solar abundance of these two elements (see Holweger 2001; Grevesse et al. 2007). Finally, chemical evolution models predict some increase in the C/H and O/H ratios in the 4.6 Gyr since the formation of the Sun (0.28 and 0.13 dex; Carigi et al. 2005). All these problems make impossible to estimate confident values of the depletion factors for C and O.

Considering the data gathered in Table 7, the C abundance is virtually the same in the nebular and shock components, although any possible small difference may be washed out due to the intrinsic relatively large error of the abundance determination of this element. In any case, only a slight increase of the C gas-phase abundance would be expected after the passage of the shock wave for a shock velocity of about 89 km s^{-1} (Jones et al. 1994).

The uncertainties in the determination of the O abundances are much lower than in the case of C and its determination does not depend on the selection of an appropriate ICF scheme. In Table 7, we see an increase of 0.06 dex in the O abundance in the shock component with respect to the nebular one. These results suggest a possible moderate decrease of the depletion for this element in the shocked material. Very recent detailed determinations of the O abundance of B-type stars in the Orion association (Simón-Díaz, in preparation) indicate that the mean O/H ratio in this zone is 8.76 ± 0.04. In principle, one would expect that this is a better reference for estimating the dust depletion in the Orion Nebula than the solar one because it corresponds to the *actual* O abundance at the same location. If we take the B-type stars determination as a reference for the total O/H ratio, the amount of O depletion in the ambient gas would be -0.17 ± 0.06 dex and -0.11 ± 0.06 dex in the gas flow. Therefore, a 30 per cent of the O tied up into dust grains would be destroyed after the passage of the shock front.

There are two other alternative methods to estimate the oxygen depletion factor. The first one can be drawn following Esteban et al. (1998). This one is based on the fact that Mg, Si and Fe form molecules with O which are trapped in dust grains. We have used Mg, Si and Fe depletions in order to obtain the fraction of O trapped in dust grains. These depletions are estimated considering the Orion gas abundances of Mg and Si given by Esteban et al. (1998), our Fe abundance for $t^2 > 0$, the O abundances derived from RLs, the stellar abundances of the Orion association of Si ($12 + \log(Si/H) = 7.41 \pm 0.10$) from Simón-Díaz (in preparation) and Mg and Fe from Przybilla et al. (2008). By assuming that O is trapped in olivine (Mg, Fe)$_2SiO_4$, pyroxene (Mg, Fe)SiO_3 and several oxides like MgO, Fe_2O_3 and Fe_3O_4 (see Savage & Sembach 1996a and references therein), we have estimated an O depletion factor of -0.10 ± 0.04 dex for the nebular component. If we consider the older stellar abundances of Si and Fe from Cunha & Lambert (1994) and the Mg/Fe ratio from Grevesse et al. (2007), this value becomes -0.08 ± 0.05, which is almost identical to that computed from the new stellar Mg, Si and Fe abundances.

The last method to obtain O depletion factors assumes that oxygen and iron are destroyed in the same fraction. The fraction of iron dust particles is calculated using the Fe abundances for $t^2 > 0$ presented in Table 7 and Fe abundance of B-type stars of the Orion association. From this assumption, and taking into account the O abundance from RLs, we have derived a depletion factor of $-0.11^{+0.11}_{-0.14}$ dex in the nebular component. Finally, we have calculated the average of the values obtained from the three methods, finding that the O depletion factor of the ambient gas is -0.12 ± 0.03. In all cases, the depletion becomes larger by about 0.08 dex if we adopt abundances for $t^2 = 0$. Additionally, the depletion factor in the shock component is smaller than in the ambient gas, probably due to gas destruction.

5.7 Photoionization models for HH 202-S

To test the role of dust destruction both in the temperature structure observed in the shock component and in the iron abundance in the gas, we have run some simple photoionization models for the nebular and the shock components. The models were constructed using CLOUDY (Ferland et al. 1998), version 07.02, and assuming a plane–parallel open geometry with density equal to the value adopted from the observations (see Table 2). We used a WM-basic (Pauldrach, Hoffmann & Lennon 2001) model stellar atmosphere, with $T_{\rm eff} = 39\,000$ K and $\log g = 4.0$, values very similar to those derived by Simón-Díaz et al. (2006) for θ^1 Ori C. The number of ionizing photons entering the ionized slab was specified using the ionization parameter, U, the ratio of hydrogen-ionizing photons to the hydrogen density. We changed the value of this parameter till the degrees of ionization (given by O^+/O^{2+}) derived for the models were close to the observed ones. The final values used for U imply similar numbers of hydrogen-ionizing photons in the nebular and shock models, with a difference of ∼40 per cent.

We have used the CLOUDY 'H II region' abundances, based on the abundances derived by Baldwin et al. (1991), Rubin et al. (1991) and Osterbrock et al. (1992) in the Orion Nebula, for all elements except iron, which we have rescaled in order to reproduce the observed [Fe III] 4658/Hβ line ratios. The models also have 'Orion' type

Table 8. Input parameters for photoionization models.

Parameter	Nebular model	Shock model A	Shock model B	Shock model C
$\log(n_e)$ (cm^{-3})	3.46	4.24	4.24	4.24
$\log(U)$	−1.95	−2.53	−2.53	−2.53
Dust	Orion	Orion	Orion	0.5 × Orion
$(Fe/H)_{gas}$	2.1×10^{-6}	2.1×10^{-6}	1.5×10^{-5}	1.5×10^{-5}

Table 9. Results of photoionization models.

Constraint	Nebular Obs.	Nebular Mod.	Shock Obs.	Shock model A	Shock model B	Shock model C
n_e (cm^{-3})	2890 ± 550	2960	17 430 ± 2360	17 540	17 670	17 650
T_e([N II]) (K)	9610 ± 390	9340	9240 ± 300	9510	9220	9210
T_e([O III]) (K)	8180 ± 200	8230	8770 ± 240	8810	8670	8640
$\log(O^+/O^{2+})$	−0.35±0.07	−0.37	0.20 ± 0.07	0.21	0.23	0.22
I([Fe III] 4658)/I(Hβ)	0.009 ± 0.001	0.010	0.110 ± 0.006	0.017	0.111	0.107

dust: graphite and silicate grains with the Orion size distribution (deficient in small grains; see Baldwin et al. 1991) and an original dust to gas mass ratio of 0.0055. For each model, we used the calculated line intensities to derive the physical conditions and the O^+ and O^{2+} abundances, following a similar procedure to the one used to derive the observational results.

We computed three shock models. Model A has similar characteristics to the nebular model except for the density, and can be used to assess the influence of this parameter on the electron temperatures. Model B has the same input parameters as model A, but with the Fe abundance multiplied by a factor of 7. Model C has the same input parameters as model B but with half the amount of dust. The input model parameters are listed in Table 8. Table 9 shows a comparison for observations and models of the physical conditions, the degree of ionization given by O^+/O^{2+}, and the [Fe III] 4658/Hβ line ratio. We can see that the nebular model reproduces well the observational constraints. As for the shock models, the increment in the density of model A is enough to explain the temperatures found for the shock component, but does not reproduce the [Fe III] flux, whereas the higher Fe abundance of model B reproduces well this flux. Model C illustrates that a reduction in the amount of dust does not change significantly the values of the chosen constraints. The introduction of grains smaller than the ones considered in the Orion size distribution of CLOUDY will lead to higher temperatures through photoelectric heating, but we do not know what grain size distribution would be suitable for the shock component.

The iron abundances in those models that reproduce the observed [Fe III] line fluxes are somewhat higher than the ones derived from the observations, but they reproduce the value of the shock to nebular abundance ratio. This can be considered a confirmation of the increment in the iron abundance in the shock component, which is most probably due to dust destruction. As it has been discussed in Section 5.6, dust destruction could also increase the gaseous abundances of other elements like carbon or oxygen and this increment will change the amount of cooling and hence the electron temperature. We ran a model where the abundances of O and C were increased by 14 per cent and found that the derived temperatures decrease by about 200 K.

6 CONCLUSIONS

We have obtained deep echelle spectrophotometry of HH 202-S, the brightest knot of the HH object HH 202. Our high spectral resolution has permitted to separate two kinematic components: the nebular component – associated with the ambient gas – and the shock one – associated with the gas flow. We have detected and measured 360 emission lines of which 352 lines were identified.

We have found a clear disagreement between the individual $c(H\beta)$ values obtained from different Balmer and Paschen lines. We outline a possible solution for this problem based on the effects of Ly-continuum pumping and ℓ-changing collisions with protons.

We have analysed the ionization structure of HH 202-S concluding that the dominant excitation mechanism in HH 202-S is photoionization. Moreover, the dependence of the $I(\lambda)_{sh}/I(\lambda)_{neb}$ ratios and the IP, the comparison of the spatio-kinematic profiles of the emission of different ions as well as the physical separation estimated of 0.14 ± 0.05 pc between HH 202-S and θ^1Ori C indicate that an ionization front is trapped in HH 202-S due to compression of the ambient gas by the shock.

We have derived a high n_e, about 17 000 cm^{-3}, and similar T_e for the low- and high-ionization zones for the shock component, while for the ambient gas we obtain an n_e of about 3000 cm^{-3}, and a higher T_e in the low-ionization zone than in the high-ionization one. We have estimated that the pre-shock gas in the immediate vicinity of HH 202 has a density of about 700 cm^{-3}, indicating that the bulk of the emission of the ambient gas comes from the background behind HH 202.

We have derived chemical abundances for several ions and elements from the flux of CELs. In particular, we have determined the Ca^+ and Cr^+ abundances for the first time in the Orion Nebula but only for the shock component. The abundance of C^{2+}, O^+ and O^{2+} have been determined using RLs for both components. The AD factor for O^{2+}, ADF(O^{2+}), is 0.35 dex in the shock component and much lower in the ambient gas component.

Assuming that the ADF and temperature fluctuations are related phenomena, we have found a $t^2(O^{2+})$ of 0.050 for the shock component and 0.016 for the nebular one. The high t^2 value of the shock component produces some apparent inconsistencies between the total abundances in both components that cast some doubts on the suitability of the t^2 paradigm, at least for the shock component. However, the fact that the values of the t^2 parameter determined from the analysis of the He I line ratios are in complete agreement with those obtained from the ADF(O^{2+}) supports that paradigm.

Finally, the comparison of the abundance patterns of Fe and Ni in the nebular and shock components and the results of photoionzation models of both components indicate that a partial destruction of dust

grains has been produced in HH 202-S after the passage of the shock wave. We estimate that the percentage of destruction of iron dust particles is of the order of 30–50 per cent.

ACKNOWLEDGMENTS

We are very grateful to the referee of this paper, J. Bally, for his comments, which have improved the scientific content of the paper. We also thank S. Simón-Díaz for providing us the stellar parameters for θ^1 Ori C. This work has been funded by the Spanish Ministerio de Ciencia y Tecnología (MCyT) under project AYA2004-07466 and Ministerio de Educación y Ciencia (MEC) under project AYA2007-63030. VL acknowledges support from MEC under project AYA2007-64712. JGR is supported by an UNAM postdoctoral grant. MR acknowledges support from Mexican CONACYT project 50359-F.

REFERENCES

Abel N. P., Brogan C. L., Ferland G. J., O'Dell C. R., Shaw G., Troland T. H., 2004, ApJ, 609, 247
Baldwin J. A., Ferland G. J., Martin P. G., Corbin M. R., Cota S. A., Peterson B. M., Slettebak A., 1991, ApJ, 374, 580
Bally J., Reipurth B., 2001, ApJ, 546, 299
Bally J., Reipurth B., 2003, AJ, 126, 893
Bally J., Licht D., Smith N., Walawender J., 2006, AJ, 131, 473
Bautista M. A., 2001, A&A, 365, 268
Bautista M. A., 2004, A&A, 420, 763
Bautista M. A., Pradhan A. K., 1998, ApJ, 492, 650
Bautista M. A., Peng J., Pradhan A. K., 1996, ApJ, 460, 372
Bautista M. A., Ballance C., Gull T., Lodders K., Martínez M., Meléndez M., 2009, MNRAS, 393, 1503
Beck-Winchatz B., Bohm K.-H., Noriega-Crespo A., 1996, AJ, 111, 346
Benjamin R. A., Skillman E. D., Smits D. P., 2002, ApJ, 569, 288
Blagrave K. P. M., Martin P. G., Baldwin J. A., 2006, ApJ, 644, 1006
Blagrave K. P. M., Martin P. G., Rubin R. H., Dufour R. J., Baldwin J. A., Hester J. J., Walter D. K., 2007, ApJ, 655, 299
Bohlin R. C., Lindler D., 1992, STScI Newsletter, 9, 19
Böhm K.-H., Matt S., 2001, PASP, 113, 158
Cantó J., Goudis C., Johnson P. G., Meaburn J., 1980, A&A, 85, 128
Carigi L., Peimbert M., Esteban C., García-Rojas J., 2005, ApJ, 623, 213
Cernicharo J. et al., 1998, Sci, 282, 462
Costero R., Peimbert M., 1970, Bol. Obser., 5, 229
Cunha K., Lambert D. L., 1994, ApJ, 426, 170
De Robertis M. M., Dufour R. J., Hunt R. W., 1987, J. R. Astron. Soc. Can., 81, 195
D'Odorico S., Cristiani S., Dekker H., Hill V., Kaufer A., Kim T., Primas F., 2000, in Bergeron J., ed., Proc. SPIE, Vol. 4005, Discoveries and Research Prospects from 8- and 10-Meter-Class Telescopes. SPIE, Bellingham, WA, p. 121
Doi T., O'Dell C. R., Hartigan P., 2004, AJ, 127, 3456
Esteban C., 2002, in Henney W. J., Franco J., Martos M., eds, Rev. Mex. Astron. Astrofis. Conf. Ser. Vol. 12, Ionized Gaseou Nebulae. UNAM, Mexico City, p. 56
Esteban C., Peimbert M., 1999, A&A, 349, 276
Esteban C., Peimbert M., Torres-Peimbert S., Escalante V., 1998, MNRAS, 295, 401
Esteban C., Peimbert M., García-Rojas J., Ruiz M. T., Peimbert A., Rodríguez M., 2004, MNRAS, 355, 229
Ferland G. J., Korista K. T., Verner D. A., Ferguson J. W., Kingdon J. B., Verner E. M., 1998, PASP, 110, 761
Froese Fischer C., Rubin R. H., 2004, MNRAS, 355, 461
García-Díaz M. T., Henney W. J., López J. A., Doi T., 2008, Rev. Mex. Astron. Astrofis., 44, 181
García-Rojas J., Esteban C., 2007, ApJ, 670, 457
García-Rojas J., Esteban C., Peimbert M., Costado M. T., Rodríguez M., Peimbert A., Ruiz M. T., 2006, MNRAS, 368, 253
Garnett D. R., Shields G. A., Peimbert M., Torres-Peimbert S., Skillman E. D., Dufour R. J., Terlevich E., Terlevich R. J., 1999, ApJ, 513, 168
Goudis C., 1982, The Orion complex: A case study of interstellar matter. Reidel, Dordrecht
Grandi S. A., 1976, ApJ, 206, 658
Grevesse N., Asplund M., Sauval A. J., 2007, Space Sci. Rev., 130, 105
Hamuy M., Walker A. R., Suntzeff N. B., Gigoux P., Heathcote S. R., Phillips M. M., 1992, PASP, 104, 533
Hamuy M., Suntzeff N. B., Heathcote S. R., Walker A. R., Gigoux P., Phillips M. M., 1994, PASP, 106, 566
Hartigan P., Raymond J., Hartmann L., 1987, ApJ, 316, 323
Henney W. J., O'Dell C. R., Zapata L. A., García-Díaz M. T., Rodríguez L. F., Robberto M., 2007, AJ, 133, 2192
Holweger H., 2001, in Wimmer-Schweingruber R. F., ed., Solar and Galactic Composition. Springer, Berlin, p. 23
Johansson S., Zethson T., Hartman H., Ekberg J. O., Ishibashi K., Davidson K., Gull T., 2000, A&A, 361, 977
Jones A. P., 2000, J. Geophys. Res., 105, 10257
Jones A. P., Tielens A. G. G. M., Hollenbach D. J., McKee C. F., 1994, ApJ, 433, 797
Kingdon J., Ferland G. J., 1995, ApJ, 442, 714
Lucy L. B., 1995, A&A, 294, 555
Luridiana V., Simón-Díaz S., Cerviño M., González Delgado R. M., Porter R. L., Ferland G. J., 2009, ApJ, 691, 1712
McKee C. F., Chernoff D. F., Hollenbach D. J., 1984, in Kessler M. F., Phillips J. P., eds, Galactic and Extragalactic Infrared Spectroscopy. Reidel, Dordrecht, p. 103
Martín-Hernández N. L. et al., 2002, A&A, 381, 606
Meaburn J., 1986, A&A, 164, 358
Meléndez M., Bautista M. A., Badnell N. R., 2007, A&A, 469, 1203
Mendoza C., 1983, in Flower D. R., ed., Proc. IAU Symp. 103, Planetary Nebulae. D. Reidel Publishing Co., Dordrecht, p. 143
Menten K. M., Reid M. J., Forbrich J., Brunthaler A., 2007, A&A, 474, 515
Mesa-Delgado A., Esteban C., García-Rojas J., 2008, ApJ, 675, 389
Mesa-Delgado A., López-Martín L., Esteban C., García-Rojas J., Luridiana V., 2009, MNRAS, 394, 693 (Paper I)
Moore C. E., 1945, A Multiplet Table of Astrophysical Interest. Princeton Univ. Obs., Princeton, NJ, p. 20
Mouri H., Taniguchi Y., 2000, ApJ, 534, L63
Nisini B., Bacciotti F., Giannini T., Massi F., Eislöffel J., Podio L., Ray T. P., 2005, A&A, 441, 159
O'Dell C. R., Doi T., 2003, AJ, 125, 277
O'Dell C. R., Henney W. J., 2008, AJ, 136, 1566
O'Dell C. R., Wen Z., Hester J. J., 1991, PASP, 103, 824
O'Dell C. R., Wong K., 1996, AJ, 111, 846
O'Dell C. R., Yusef-Zadeh F., 2000, AJ, 120, 382
O'Dell C. R., Hartigan P., Lane W. M., Wong S. K., Burton M. G., Raymond J., Axon D. J., 1997, AJ, 114, 730
Osterbrock D. E., Tran H. D., Veilleux S., 1992, ApJ, 389, 305
Pauldrach A. W. A., Hoffmann T. L., Lennon M., 2001, A&A, 375, 161
Peimbert M., 1967, ApJ, 150, 825
Peimbert M., 1995, in Williams R., Livio M., eds, The Analysis of Emission Lines. Cambridge Univ. Press, Cambridge, p. 165
Peimbert M., Costero R., 1969, Bol. Obs. Tonantzintla y Tacubaya, 5, 3
Peimbert M., Peimbert A., 2006, in Barlow M. J., Méndez R. H., eds, Proc. IAU Symp. 234, Planetary Nebulae in our Galaxy and Beyond. Cambridge Univ. Press, Cambridge, p. 227
Peimbert M., Sarmiento A., Fierro J., 1991, PASP, 103, 815
Peimbert M., Peimbert A., Ruiz M. T., 2000, ApJ, 541, 688
Peimbert A., Peimbert M., Luridiana V., 2002, ApJ, 565, 668
Peimbert M., Torres-Peimbert S., Ruiz M. T., 1992, Rev. Mexicana Astron. Astrofis., 24, 155
Porter R. L., Bauman R. P., Ferland G. J., MacAdam K. B., 2005, ApJ, 622, L73
Porter R. L., Ferland G. J., MacAdam K. B., 2007, ApJ, 657, 327
Przybilla N., Nieva F. M., Butler K., 2008, ApJ, 688, L103

Quinet P., 1996, A&AS, 116, 573
Raga A. C., Cantó J., De Colle F., Esquivel A., Kajdic P., Rodríguez-González A., Velázquez P. F., 2008, ApJ, 680, L45
Reipurth B., Bally J., Fesen R. A., Devine D., 1998, Nat, 396, 343
Riera A., Mampaso A., Vilchez J. M., Phillips J. P., 1989, A&A, 210, 351
Rodríguez M., 1999, A&A, 348, 222
Rodríguez M., 2002, A&A, 389, 556
Rodríguez M., Rubin R. H., 2005, ApJ, 626, 900
Rosado M., de La Fuente E., Arias L., Le Coarer E., 2002, Rev. Mexicana Astron. Astrofis. Conf. Ser., 13, 90
Rubin R. H., Simpson J. P., Haas M. R., Erickson E. F., 1991, ApJ, 374, 564
Rubin R. H., Martin P. G., Dufour R. J., Ferland G. J., Blagrave K. P. M., Liu X.-W., Nguyen J. F., Baldwin J. A., 2003, MNRAS, 340, 362
Ruiz M. T., Peimbert A., Peimbert M., Esteban C., 2003, ApJ, 595, 247
Savage B. D., Sembach K. R., 1996a, ARA&A, 34, 279
Savage B. D., Sembach K. R., 1996b, ApJ, 470, 893
Sawey P. M. J., Berrington K. A., 1993, At. Data Nucl. Data Tables, 55, 81
Shaw R. A., Dufour R. J., 1995, PASP, 107, 896
Simón-Díaz S., Herrero A., Esteban C., Najarro F., 2006, A&A, 448, 351
Smith N., Bally J., Brooks K. J., 2004, AJ, 127, 2793
Smith N., Bally J., Shuping R. Y., Morris M., Kassis M., 2005, AJ, 130, 1763
Stasińska G., 1978, A&A, 66, 257
Storey P. J., Hummer D. G., 1995, MNRAS, 272, 41
Tsamis Y. G., Barlow M. J., Liu X.-W., Danziger I. J., Storey P. J., 2003, MNRAS, 338, 687
Turnshek D. A., Bohlin R. C., Williamson R. L., Lupie O. L., Koornneef J., Morgan D. H., 1990, AJ, 99, 1243
Verner E. M., Verner D. A., Baldwin J. A., Ferland G. J., Martin P. G., 2000, ApJ, 543, 831
Walter D. K., Dufour R. J., Hester J. J., 1992, ApJ, 397, 196
Welty D. E., Hobbs L. M., Lauroesch J. T., Morton D. C., Spitzer L., York D. G., 1999, ApJS, 124, 465
Zhang H., 1996, A&AS, 119, 523
Zhang H. L., Pradhan A. K., 1997, A&AS, 126, 373

This paper has been typeset from a TEX/LATEX file prepared by the author.